Journal of
Materials Chemistry A

ROYAL SOCIETY OF CHEMISTRY

REVIEW

View Article Online
View Journal | View Issue

Cite this: *J. Mater. Chem. A*, 2022, **10**, 19278

Published on 14 giugno 2022. Downloaded on 16/07/2024 00:14:22.

Current state-of-the-art characterization methods for probing defect passivation towards efficient perovskite solar cells

Duoling Cao,†[a] Wenbo Li,†[a] Xu Zhang,*[a] Li Wan, *[a] Zhiguang Guo,[a] Xianbao Wang, [a] Dominik Eder [b] and Shimin Wang[a]

Received 21st March 2022
Accepted 31st May 2022

DOI: 10.1039/d2ta02263j

rsc.li/materials-a

Various types of imperfections/defects in metal halide perovskite (MHP) light-absorbing layers and/or at relevant interfaces have indelible effects on perovskite solar cells (PSCs) in terms of performance, stability, and scalability. So far, some effective defect-passivation strategies and agents have successfully been applied to reduce defects in MHPs to improve film quality and device properties for future commercialized long-term stable large-scale PSCs. Characterization methods play an important role in clarifying the mechanistic understanding of defect passivation in MHPs, allowing the development of more efficient passivation strategies. Therefore, new advanced measurements of defect passivation, especially some *in situ* techniques that are different from conventional characterization tools, were reviewed in this paper aiming to provide useful guidelines for further continuously promoting MHP and PSC research.

1. Introduction

Over the past few years, metal halide perovskites (MHPs) have succeeded as one of the new wonder materials not only for traditional areas of photovoltaics,[1] light-emitting diodes (LEDs),[2] photodetectors and photocatalysis,[3,4] but also for many novel potential applications, such as X-ray imaging sensors,[5,6] flexible scanners,[7] photorechargeable ion batteries (IBs),[8,9] biomedical detectors[10–12] and information memory.[13–15] Metal halide perovskites with bulk 3D form have a general chemical formula of ABX_3, where A is an organic or inorganic monovalent cation (typically methylammonium, formamidinium or cesium), B is a divalent metal ion (Sn^{2+}, Ge^{2+}, or Pb^{2+}), and X is a halide anion (Cl^-, Br^-, or I^-). Significantly, the most impressive development has so far been achieved undoubtedly in perovskite-light absorber based solar cells (PSCs) with the certified power conversion efficiency (PCE) reaching 25.5%,[16] since being initially reported in 2009. The superior photovoltaic

[a]Key Laboratory for the Green Preparation and Application of Functional Materials, Ministry of Education, Hubei Key Laboratory of Polymer Materials, Hubei Collaborative Innovation Center for Advanced Organic Chemical Materials, Faculty of Materials Science and Engineering, Hubei University, Wuhan 430062, PR China. E-mail: wanli@hubu.edu.cn; wanli1983_3@aliyun.com; xuzhang@hubu.edu.cn

[b]Institute of Materials Chemistry, Technische Universität Wien, Getreidemarkt 9/165, 1060 Vienna, Austria

† The first two authors contributed equally.

Duoling Cao received her B.Sc. degree in Chemistry from Yangtze Normal University in 2020 and now is a master's student of the School of Materials Science and Engineering, Hubei University, China. She is under the supervision of Associate Professor Dr Li Wan, doing research on designing the interface structure and carrier transport optimization of carbon counter electrode based perovskite solar cells.

Wenbo Li received his B.Eng. degree in Polymer Materials Science and Engineering from Hubei University in 2020. He is currently a master's student of the School of Materials Science and Engineering, Hubei University, China under the supervision of Associate Professor Dr Li Wan. His research focuses on performance optimization of all-inorganic perovskite solar cells.

This journal is © The Royal Society of Chemistry 2022

Published on 14 giugno 2022. Downloaded on 16/07/2024 00:14:22.

performances of PSCs have mainly been attributed to the excellent optoelectronic properties of MHPs, such as high optical absorption coefficients, long carrier diffusion length, low exciton binding energy and tunable bandgaps.[17–20] However, lab-prepared single-junction PSCs are still far from the thermodynamic PCE limit and large-scale application despite their promising high PCE. One main reason for this has to do with the tremendous amounts of various types of imperfections/defects present in the perovskite layer and/or at relevant interfaces issuing from perovskite crystallization/composition and device/module fabrication processes due to the inherently 'softer' ionic crystal characteristics of MHPs.[21–24] The existence of such defects in MHPs could result in ion migration, non-radiative recombination, hysteresis, charge trapping, charge scattering and even degradation of perovskites or metal electrodes, thereby negatively influencing the performance, stability, and scalability of PSCs.[25] Recently, some effective defect-passivation strategies and agents like interface modification,[26,27] and additive,[28,29] solvent[30,31] and composition engineering[32,33] have successfully been developed for reducing defects in MHPs to improve the film quality and device properties by inhibiting non-radiative recombination, as well as prolong the carrier lifetime aiming for long-term stable and large-scale PSCs.[34]

Sharp tools make good work. Obviously, it is the results of characterization methods that can mainly help us to acquire deep mechanistic understanding of the fundamentals involved in the defect passivation of MHPs, which can then guide in choosing optimal defect passivation strategies to prepare MHP-based devices with high performance and long-term stability. So far, various techniques based on spectroscopy,[35] microscopy, synchrotron and *in situ* neutron diffraction have been successfully employed for evaluating the chemical, morphological, structural, and optoelectronic properties of MHPs before and after the defect passivation. These tools have also been useful in elucidating the root causes of the E_{loss}, degradation mechanisms and low scalability of the PSCs. However, conventional methods based on X-ray, laser, or electron beam-based sources may accelerate the degradation of MHPs by a localized temperature increase, thereby producing severe artifacts during long-term characterization. Also, the current density–voltage (*J*–*V*) and monochromatic incident photon-to-electron conversion efficiency (IPCE) characterization of full photovoltaic devices under light illumination may also give rise to hysteresis or phase separation due to ion migration and charge accumulation during measurement.[35] Therefore, conventional characterization methods require optimization and suitable new *in situ* imaging techniques or *operando* measurement approaches also need to be developed for MHP and PSC research. Typically, capacitance measurements like drive-level capacitance profiling (DLCP),[36] space-charge-limited-current (SCLC)[37,38] and deep-level transient spectroscopy (DLTS),[39] as well as spectrometric characterization methods like steady-state PL emission (ssPL)[40,41] along with *in situ* techniques are new emerging characterization tools that might be used for an in-depth understanding of PSC materials (Fig. 1).

Meng *et al.*[35] reviewed some useful characterization methods used for MHPs and PSCs. Other published literature[42,43] reviews/articles have briefly introduced commonly used techniques for the characterization of defects only mentioned in several paragraphs. However, timely reviews systematically focused on new measurements of defect passivation are still lacking. Moreover, a summary of *in situ* and *operando* characterization approaches for defect passivation is also needed. Therefore, specific reviews regarding this topic are imperative and urgently needed for providing useful guidance for further continuously boosting the

Dr Xu Zhang received her PhD degree in Physical Chemistry from the University of the Chinese Academy of Sciences in 2021. Now, she is working as a Lecturer at the School of Materials Science and Engineering, Hubei University, China. Her research focuses on perovskite materials, thin films, optoelectronics, etc.

Dr Li Wan is an Associate Professor of new energy materials and devices at the School of Materials Science and Engineering, Hubei University, China. She obtained her PhD in Materials Science at Hubei University in 2011, working on low-cost carbon counter electrodes for dye sensitized solar cells. She worked as a Visiting Scholar at TU Wien, Austria from 2016 to 2017 and Shaanxi Normal University, China from 2018 to 2019. Her main research interests include high efficiency and low-cost photovoltaic devices like organic solar cells and perovskite solar cells, nano-carbon materials (carbon nanotubes and graphene), and composites for optoelectronic applications. Deep understanding of electrified interfaces is crucial to energy devices. Therefore, she has started to focus on researching in situ electrochemical characterization of electrified interfaces.

Published on 14 giugno 2022. Downloaded on 16/07/2024 00:14:22.

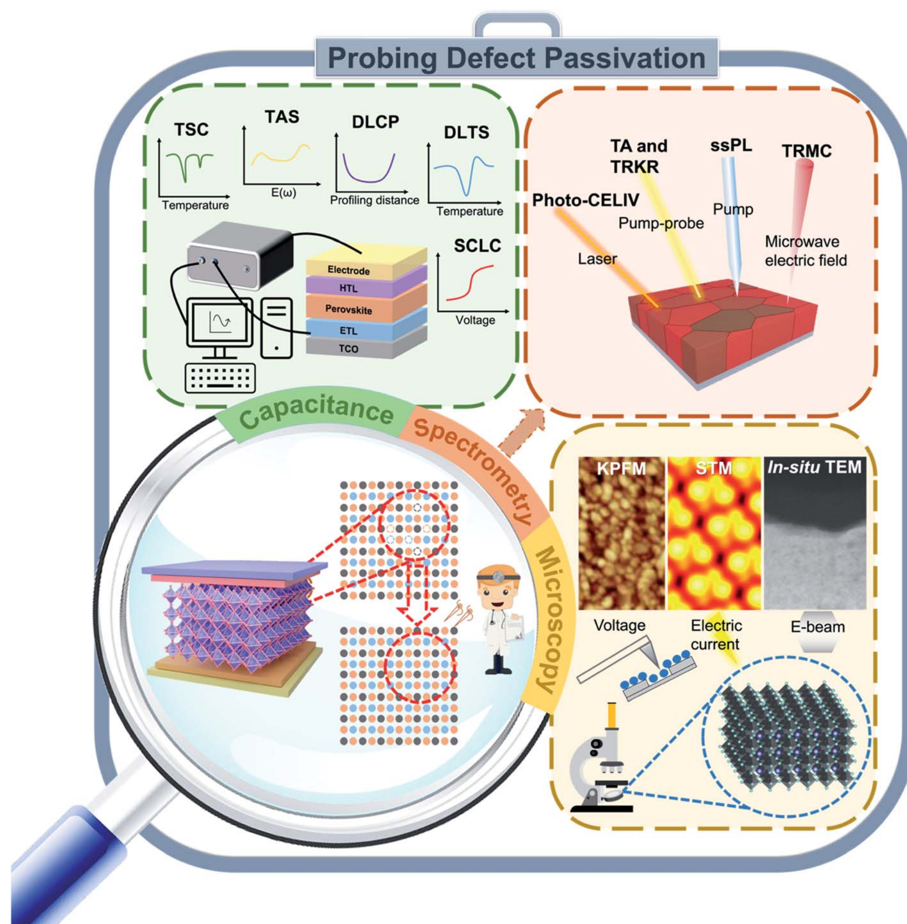

Fig. 1 Summary of new characterization measurements applied to probing defect passivation in perovskite solar cell research. The inserted KPFM, STM, and *in situ* TEM images were reproduced with permission:[141] copyright 2019, Elsevier.[130] Copyright 2015, American Chemical Society.[135] Copyright 2016, American Chemical Society.

development of PSCs. In the present review, we first give a short introduction to defects in MHPs, their influences on PSCs and progress in defect passivation. We then focus on summarizing and categorizing the current state-of-the-art advanced characterization techniques used for probing defect passivation so far, which are different from conventional characterization tools. Their limitations are also briefly discussed.

2. Characterization techniques for defect passivation

Different from ideal crystals, actually prepared MHPs have an incomplete crystal structure with various forms of defects. Point defects are the main form of defects in MHP crystals. Recently, many theoretical calculations have investigated the defect states of the most commonly used $MAPbI_3$ perovskites with the crystal structure of ABX_3 (Fig. 2a). Note that $MAPbI_3$ native point defects include V_{MA}, V_{Pb} and V_I vacancies; interstitial MA_i, Pb_i and I_i; *trans*-substituted Pb_I, I_{Pb}, I_{MA} and MA_I; and cationic substituents Pb_{MA} and MA_{Pb} [44] (Fig. 2b). It is generally considered that defects in perovskites with low formation energies have shallower energy levels near the valence band maximum or conduction band minimum, while defects with deep formation energies have higher formation energies in the band gap[45] (Fig. 2c–e). Density functional theory (DFT) calculations confirmed that the energy levels of these defects in $FAPbI_3$ are similar to those in $MAPbI_3$, except that the antisites (FA_I and I_{FA}) create deep energy levels in $FAPbI_3$ due to their lower formation energies.[46] Li *et al.* found that in the α-phase of $CsPbI_3$, under Pb-rich conditions, the energies of V_{Pb} and V_I formation were the lowest among all acceptor and donor conditions, respectively.[47] Huang *et al.* showed that most of the intrinsic defects in the δ-phase $CsPbI_3$ induce deeper transition levels compared to γ-phase $CsPbI_3$.[48] More recently, Dunfield *et al.* linked the fault tolerance to the structural stability for perovskite materials.[49] The structural tolerance coefficients of $MAPbI_3$, $CsPbBr_3$,[50] $CsSnI_3$,[51] and $MAPbBr_3$ [52] are about 0.82–0.85, whereas those of $FAPbI_3$, $CsPbI_3$, $FASnI_3$, and $MASnI_3$ [53] are outside this range. For polycrystalline perovskite films used in PSCs, other-dimensional (2D and 3D) defects like grain boundaries (GBs) may exist. Point defects would generate transition levels made mainly of Fermi level sites located near the conduction band minimum (CBM) or valence band maximum (VBM) representing shallow-level defect traps or within the forbidden band

 This journal is © The Royal Society of Chemistry 2022

Published on 14 giugno 2022. Downloaded on 16/07/2024 00:14:22.

(deep-level defect traps) of MHPs. These transition levels may introduce charge recombination centers (traps) to trap free electrons or holes. Meanwhile, shallow-level defect traps with low charge recombination rates could affect the charge mobility to some extent. Deep-level defect traps, also known as Shockley–Read–Hall (SRH) recombination centers, may be annihilated with the anti-charge like non-radiative recombination process, thereby releasing part or all of the electrical energy in the form of phonons into adjacent lattices.[45,54,55] This process can be detrimental to efficient charge extraction in PSCs. Impurity defects of extrinsic ions, such as Li^+, Na^+, and H^+ issuing from the hole transport layer (HTL),[56,57] deposited counter electrodes, and many other raw materials of PSCs, could migrate across the perovskite layer and strongly affect the charge separation at the charge transport layer (CTL)/perovskite interface and cause current–voltage hysteresis in PSCs. 2D defects, including GBs and surface defects, may reduce the bandgap and increase the coupling,[58,59] thereby accelerating non-radiative charge recombination. 3D defects rely on the presence of metallic lead clusters in perovskite films generated by imbalanced I/Pb stoichiometry similar to the formation of halide vacancies. The concentration of metallic Pb has been demonstrated to be closely related to the density of states above the VBM and close to the Fermi level. Reduction of metallic Pb concentration may reduce such density of states and improve the photoluminescence quantum efficiency of perovskite films.[60,61] In tin based PSCs, high concentrations of SnI_2 and SnI_4 will induce nonradiative recombination and shorten the carrier lifetime under the Sn-rich environments, while a high concentration of V_{Sn} electron acceptor defects can lead to a large number of background holes[62] under tin-deficient conditions. The non-radiative recombination caused by defects may diminish the steady-state electron/hole density, charge lifetime, and charge diffusion length in PSCs, thereby resulting in severe degradation of PSC performance.

With the gradual rise of the PCE, the long-term stability of PSCs has been paid increasing attention. The main factors affecting the stability of PSCs include the crystal structure stability of MHPs, the interface and device structural stability, and degradation caused by environmental agents like water, oxygen, heat, light, and electricity.[63–65] Essentially, all of these factors are closely related to the defects present in MHPs. For

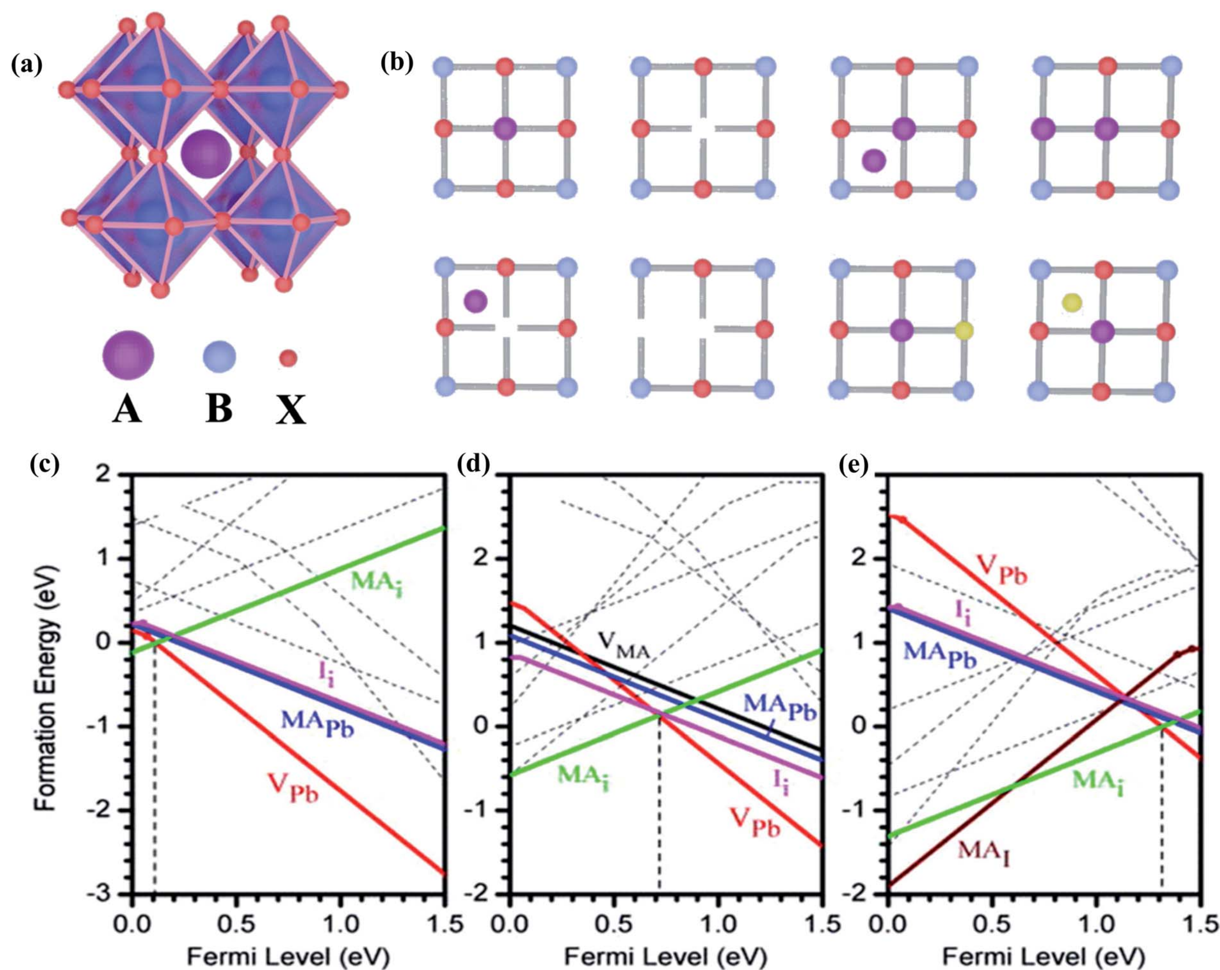

Fig. 2 (a) Schematic representation of the ABX_3 unit cell. (b) Illustration of a perfect lattice, vacancy, interstitial, anti-site substitution, Frenkel defect pair, Schottky defect pair, substitutional, and interstitial impurity group. (c–e) The calculated formation energies of intrinsic point defects in $MAPbI_3$ at different chemical potentials. Reproduced with permission:[45] copyright 2014, AIP Publishing LLC.

instance, exposure to humidity would cause water and oxygen molecules to penetrate into MHPs through the GBs in polycrystalline perovskite films, causing degradation of the perovskite layer.[66,67] Under light exposure, the O_2 present forms superoxide (O_2^-), leading to deprotonation reactions accelerating the decomposition of MHPs.[68] In the actual outdoor working environment (high temperature, water vapor, oxygen, *etc.*), the decomposition of perovskites is mainly reflected in the promotion of phase transition and perovskite ion migration, as well as the sensitivity to the external environment at high temperature. Additionally, the electric field may induce rapid migration of ions.[69,70]

Published on 14 giugno 2022. Downloaded on 16/07/2024 00:14:22.

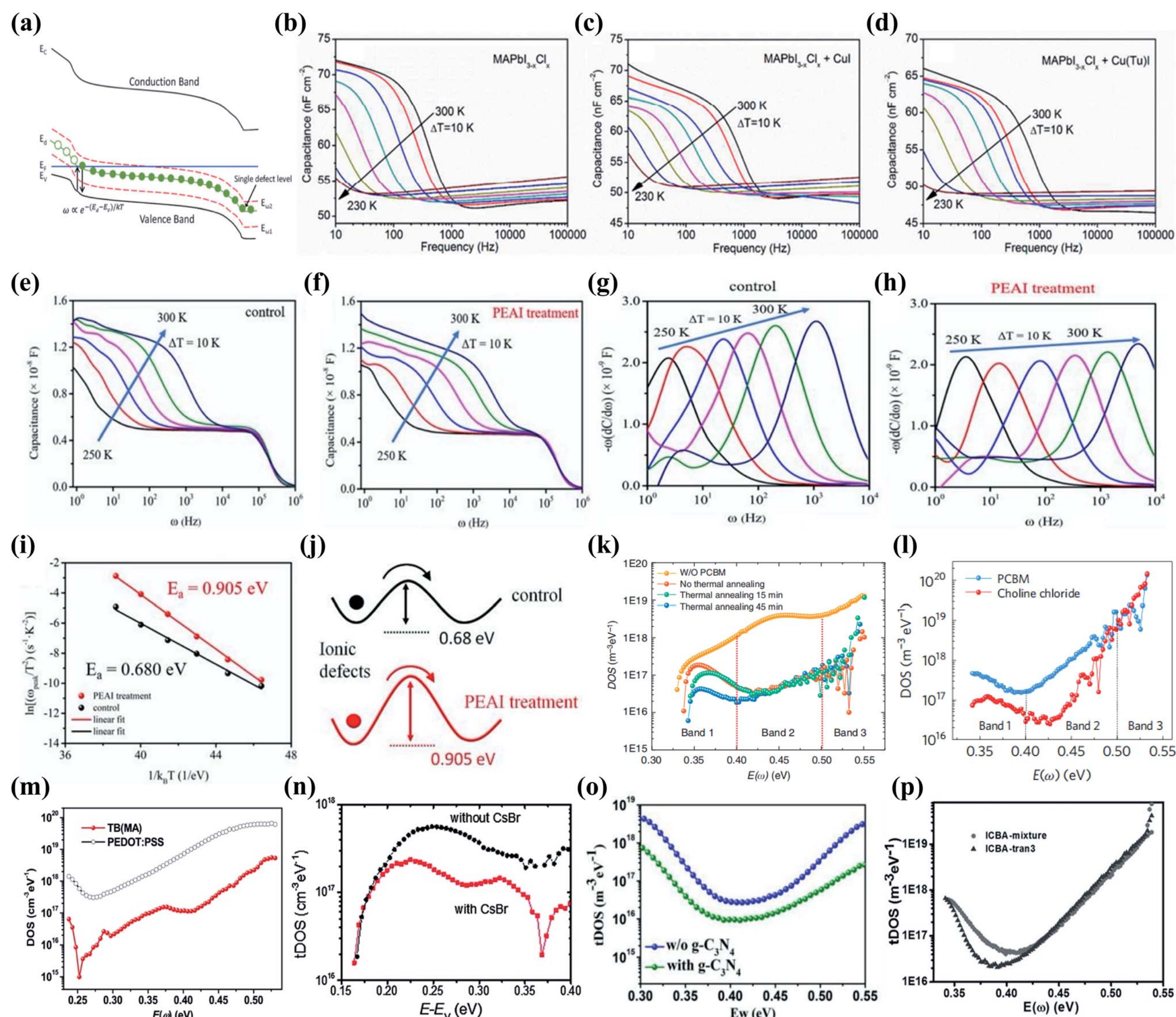

Fig. 3 (a) A schematic band diagram of a p-type semiconductor junction with a single trap level E_d and two measurement energies $E_{\omega 1}$ and $E_{\omega 2}$. Reproduced with permission:[80] copyright 2015, Royal Society of Chemistry. Admittance spectra of (b) the reference PSC without TSP and the device with (c) CuI or (d) Cu(Tu)I as the TSP. Reproduced with permission:[84] copyright 2017, American Chemical Society. Admittance spectra of WBG PSCs (e) without (the control) and (f) with the PEAI treatment. The derivative of admittance spectra of (g) the control device and (h) the device with the PEAI treatment. (i) Arrhenius plots of the characteristic transition frequencies derived from the admittance spectra. (j) Schematic of the energy barrier for ion movement in the control and the device with PEAI treatment. Reproduced with permission:[85] copyright 2020, American Chemical Society. (k) tDOS for devices without PCBM (orange), with PCBM but no thermal annealing (red), with 15 min thermal annealing of PCBM (green), and 45 min thermal annealing of PCBM (blue). Reproduced with permission:[82] copyright 2014, Springer Nature. (l) Trap density of states obtained by thermal admittance spectroscopy for devices with PCBM (blue), and choline chloride passivation layers (red). Reproduced with permission:[86] copyright 2017, Springer Nature. (m) TAS plots of the PSC devices. Reproduced with permission:[87] copyright 2019, Elsevier. (n) Trap density of states (tDOS) for devices without CsBr (black) and with CsBr modification (red). Reproduced with permission:[88] copyright 2013, Royal Society of Chemistry. (o) tDOS characterization for the PSCs based on control $MAPbI_3$ and g-C_3N_4 modified $MAPbI_3$ films. Reproduced with permission:[89] copyright 2012, Royal Society of Chemistry. (p) Those of the WBG $MAPbI_xBr_{3-x}$ perovskite solar cells based on ICBA-mixture and ICBA-tran3. Reproduced with permission:[90] copyright 2017, Wiley-VCH.

 This journal is © The Royal Society of Chemistry 2022

Published on 14 giugno 2022. Downloaded on 16/07/2024 00:14:22.

The presence of defects in perovskite thin films not only directly affects the photovoltaic performance of PSCs through non-radiative recombination of photogenerated carriers but also reduces the long-term stability of MHPs and PSCs. Hence, various passivation strategies have so far been successfully applied to improve the efficiency and stability of PSCs. These methods include the introduction of additives, interface modification, component regulation, solvent engineering, single-crystal engineering,[71–73] and electrochemical deposition.[74–77] The passivation route relies on applying certain chemicals to react with surface components for deactivating their electronic or chemical activities. This approach generally reduces MHP defects and improves the device performance.[42,43,78] Defect passivation could also change the contact resistance at the CTL/perovskite interface. The addition of passivation agents to perovskite precursors may improve the film morphology in terms of fewer pinholes, thereby increasing the filling factor of PSCs.

Combined with defect passivation strategies, many commonly used characterization techniques including microscopy, spectroscopy and electrical measurements have promoted PSC research. The clarifications provided by these tools about the structure, morphology, chemical composition, and optoelectronic and electrical properties of MHPs help further improve the quality of perovskite layers and the performance of PSCs. Since the performance and stability of PSCs are seriously affected by defects in perovskite layers, advanced characterization methods are required for a deep investigation of the defect characteristics of perovskite layers. Thus, several new characterization techniques for MHP trap states (density and energy levels) were reviewed in this article to gain a better understanding of the defect passivation mechanism in MHPs.

2.1 Capacitance measurements

Charged defects are equivalent to a localized capacitor, where trapped charges influence not only the electrical properties but also the capacitance characteristics of the semiconductor. Therefore, the features of a defect can be deduced by tracing the changes in capacitance under alternating current (AC) voltage.

2.1.1 Thermal admittance spectroscopy (TAS). Thermal admittance spectroscopy (TAS) is an established and effective technique broadly applied for measuring the defect density in solar cells (SCs). This includes both shallow- and deep-level defects measured by tracing the junction capacitance related to the defect density and its effectiveness as a dopant. TAS measurements at various temperatures are commonly used to reveal the defect density and energy distribution within the band gap in a semiconductor.[79] In typical p–n junction SCs, the capacitance mainly originates from the charging/discharging of defects as a function of frequency change under AC voltage. Meanwhile, defect occupancy of the semiconductor is determined by the position of the Fermi level. As shown in Fig. 3a, electron traps below the Fermi level are assumed to be filled with photo-generated electrons. Upon changes in the frequency of AC voltage, the corresponding traps may release their charge within the AC period, thereby contributing to the admittance.[80,81] The release of the charge depends not only on the energy depth of the defect but also on the temperature since the charge could thermally be activated and released to contribute to the admittance signal. Therefore, defect traps with different activation energies (E_a) at different modulated AC frequencies and temperatures are related to the junction capacitance.

The energy of the defect energy level E_a at frequency ω and the characteristic attempt-to-escape frequency ω_0 can be expressed according to eqn (1) and (2):[82]

$$E_a = E_d - E_v \tag{1}$$

$$\omega_0 = \beta T^2 \exp\left(-\frac{E_a}{k_B T}\right) \tag{2}$$

where E_v, E_d, ω_0, and β are the VBM energy level, energy depth of the defect, attempt-to-escape frequency, and a temperature-dependent parameter, respectively.

Below E_a, defect traps could capture or emit charges and contribute to the capacitance. The defect density may derive from the angular frequency-dependent capacitance using eqn (3):[82]

$$n_{trap}(E_a) = -\frac{V_{bi}}{qW}\frac{dC}{d\omega}\frac{\omega}{k_B T} \tag{3}$$

where C and ω represent the capacitance and angular frequency, respectively. V_{bi} and W are the built-in potential and depletion width of the target material extracted from capacitance–voltage measurements and Mott–Schottky analysis, respectively.

Typical analyses of capacitance–voltage scans for Schottky junctions are often based on depletion approximation by assuming no free charges at the junction in the space charge region. In this case, the charge in this region entirely originates from dopant atoms or molecules, and depletion width W can be expressed as:[83]

$$W = \frac{\varepsilon_0 \varepsilon_r A}{C} \tag{4}$$

where ε_r and A are the relative dielectric constant and contact area, respectively.

Ye *et al.* compared the defect passivation effect of CuI and Cu(Tu)I in $MAPbI_{3-x}Cl_x$ by the TAS method.[84] The calculations of temperature-dependent admittance spectra of devices without and with trap state passivation (TSP) at various temperatures (T = 230 K to 300 K) from 10 to 105 Hz in the dark demonstrated that Cu(Tu)I had a better defect passivation effect than CuI (Fig. 3b–d). Arrhenius plots of characteristic transition frequencies correspond to admittance derivatives and the calculated E_a of pure perovskites and perovskites–Cu(Tu)I are 0.318 and 0.388 eV, respectively. The higher E_a value in the latter indicates that the ion migration in the perovskite layer is significantly suppressed after treatment with Cu(Tu)I. Chen *et al.* used TAS measurements on wide-bandgap (WBG) $FA_{0.8}Cs_{0.2}Pb(I_{0.7}Br_{0.3})_3$ perovskite-based PSCs without and with the phenethylammonium iodide (PEAI) treatment to elucidate the suppression of ion migration.[85] Their data showed that

Published on 14 giugno 2022. Downloaded on 16/07/2024 00:14:22.

suppression of mobile ionic defects might reduce the formation of charge defects acting as non-radiative recombination centers. Their recent work revealed the usefulness of low-frequency capacitance measured by the TAS technique for estimating the activation energy (E_A) of ion motion in perovskite absorber layers. The TAS spectra of PSCs without and with PEAI treatment were measured from 250 to 300 K in the dark (Fig. 3e and f) and the derivative of the capacitance–frequency spectra was used to obtain the characteristic transition frequency values (ω_{peak}) (Fig. 3g and h). The E_a values were calculated by fitting the corresponding Arrhenius plots using the formula $\omega_{peak} = \beta T^2 \exp(-E_a/kT)$, where β refers to a temperature-related prefactor. Their findings indicated an E_a of 0.905 eV obtained by the device subjected to PEAI treatment. This value was higher than that of the control device (0.680 eV) (Fig. 3i and j). The higher E_a value indicates that the ion migration in the perovskite layer is significantly suppressed after treatment with PEAI. Suppression of mobile ion defects is also expected to reduce the formation of charge defects, which can act as nonradiative recombination centers. The substantially higher E_a indicated significantly suppressed ion migration in the perovskite layer after PEAI treatment. Shao *et al.* used a typical curve of trap density of states (tDOS) *versus* defect energy level E_a to investigate defect passivation by PCBM in $MAPbI_3$ based PSCs.[82] They found that E_a below 0.4 eV (band 1, 0.35–0.40 eV) could be assigned to a relatively shallow-level defect trap, while E_a above 0.4 eV (band 2 and band 3) may be indexed to deeper levels (Fig. 3k). The PSCs containing a PCBM layer without thermal annealing illustrated significantly reduced tDOS at band 2 and band 3. By comparison, PSCs containing a PCBM layer and subjected to annealing revealed efficiently more reduced shallow-level defect traps. Therefore, the deep-level defect trap located at the $MAPbI_3$ film surface was effectively passivated by PCBM without thermal annealing. The even deeper shallow-level defect traps found in $MAPbI_3$ films can only be passivated by diffusion of PCBM into the $MAPbI_3$ inner layer. Zheng *et al.* utilized the TAS method to clarify the better passivation effect of choline chloride when compared to PCBM by considering both cationic and anionic defects in MHPs during passivation strategies.[86] The obtained device with choline chloride layers showed the lowest tDOS over the whole trap depth region (Fig. 3l), while the low tDOS in the deeper trap region of 0.40–0.52 eV was assigned to defects at the film surface. Furthermore, the density of shallower trap states in the choline-chloride-passivated devices (0.35–0.40 eV) assigned to traps at GBs was about 3-fold smaller than that in PCBM-passivated devices, indicating the diffusion of choline chloride and passivation of the GBs.

Overall, defects are very important and are thus further investigated since defects in the $MAPbI_3$ perovskite layer change significantly. For instance, Zhang *et al.* studied the tDOS through TAS measurements. The tDOS values for a TB(MA) modified PSC with a backbone composed of a 2,5-dialkoxy-1,4-phenylene unit and thiophene unit, and side-chain end-capped by $-SO_3-$ MA^+ were found to be more than one order of magnitude lower in the entire energy range.[87] The exact densities of shallow- and deep-level defect traps were calculated to be 9.59×10^{15} cm^{-3} and 1.94×10^{17} cm^{-3} for the TB(MA) modified device, respectively. By comparison, 2.43×10^{17} cm^{-3} and 5.09×10^{18} cm^{-3} were recorded for the control device (Fig. 3m), respectively. Thus, fewer interface defects were obtained by the TB(MA) passivator. Li *et al.* further examined the energetic profile of tDOS at the $MAPbI_{3-x}Cl_x$ perovskite/TiO_2 interface by performing TAS on complete photovoltaic devices. Their data revealed a decline in tDOS from 5.0×10^{16} cm^{-3} (without CsBr) to 2.0×10^{16} cm^{-3} (with CsBr) (Fig. 3n), confirming enhanced electronic contact between perovskites and c-TiO_2 through CsBr modification and resulting in improved interface stability.[88] Liao *et al.* measured TAS for quantifying the tDOS of devices fabricated with and without the g-C_3N_4 additive (Fig. 3o). The g-C_3N_4 modified device illustrated remarkably reduced tDOS in the deeper trap region (0.40–0.55 eV) corresponding to defects at the film surface, as well as a shallower trap region (0.30–0.40 eV) assigned to traps at GBs.[89] This confirmed that doping of g-C_3N_4 might enlarge the grain size and improve the crystallinity, thereby passivating the defects. Moreover, the soft and mechanically flexible framework of g-C_3N_4 could passivate poorly coordinated ions at the GBs or on $MAPbI_3$ film surfaces. Lin *et al.* measured the TAS of tDOS in devices composed of two different electron transfer layers (ETLs) to figure out the origin of the charge-carrier lifetime enhancement by replacing the indene-C60 bisadduct (ICBA)-mixture with ICBA-tran3.[90] To this end, a simple method was applied to reduce the energy disorder by isolating the isomer ICBA-tran3 from the as-synthesized ICBA-mixture. The obtained density of defect states ranged from 1×10^{16} to 1×10^{19} m^{-3} for both types of PSCs. The tDOS was almost identical for the ICBA-tran3 and ICBA-mixture based WBG $MAPbI_xBr_{3-x}$ PSCs with values estimated to be 0.42–0.55 eV (Fig. 3p). The tDOS values of the shallower traps (0.35–0.42 eV) in ICBA-mixture based devices were larger than those of ICBA-tran3 devices, revealing a slightly weaker passivation effect by the ICBA-mixture.

2.1.2 Drive-level capacitance profiling (DLCP). TAS has widely been used for analysis of tDOS but is unsuitable for profiling the spatial distribution of tDOS in semiconductor films or crystals. Alternatively, Ni *et al.* demonstrated the usefulness of the drive-level capacitance profiling (DLCP) method for characterizing the spatial and energetic distributions of carrier and trap densities in PSCs.[36] In Fig. 4a, X denotes the distance from the junction barrier (n^+–p junction) where the traps may be able to dynamically change their charge states as a function of AC bias δV, and δX refers to the differential change in X with respect to δV. The DLCP method exploits the dependence of junction capacitance on the magnitude of AC voltage (δV) to yield the trap density at X position.[91,92] The DLCP technique also allows deriving the energetic distribution (E_ω) of trap states by tuning the frequency of AC bias or temperature (T), similar to TAS measurements. In this way, both the trap density and trap depth could be extracted. The trap states at different positions in real space might also be obtained by changing the DC bias applied to the depletion region of the junction. The specific procedures for analyzing tDOS with the DLCP method can be found in related literature.

Ni *et al.* obtained profiling of spatial and energetic distributions of trap states in metal halide perovskite single-

 This journal is © The Royal Society of Chemistry 2022

Published on 14 giugno 2022. Downloaded on 16/07/2024 00:14:22.

crystalline and polycrystalline solar cells.[36] Their results suggested trap densities in single crystals varying by five orders of magnitude, with the lowest value estimated to be 2×10^{11} per cubic centimeter, and most deep traps were located at crystal surfaces. Also, symmetric distribution of the trap density was observed (Fig. 4b), consistent with the structural symmetry of the double-side polished $MAPbI_3$ single crystal. The spatial profiling of trap densities in $MAPbI_3$ single crystals was also performed by DLCP and the data illustrated about 10-fold greater trap density near the interface region than inside the $MAPbI_3$ single crystal. Thus, dangling bonds at the surface of the crystal formed charge traps. To gain a better understanding of the relationship of trap density and distribution, DLCP measurements were also conducted on devices with the ITO/PTAA/$MAPbI_3$ (39 μm)/C_{60}/BCP/Cu structure based on a typical $MAPbI_3$ thin single crystal synthesized by a space-confined growth method (Fig. 4c). The increase in carrier density with the decrease in AC frequency confirmed the existence of charge traps contributing to junction capacitance at low AC frequencies (large E_ω) in the $MAPbI_3$ thin single crystal. The trap density distribution in the $MAPbI_3$ thin single crystal synthesized by the space-confined method was different from that in the bulk crystal. The trap density in the $MAPbI_3$ thin single-crystal varied by up to 5-fold, and the trap density near both surfaces was 2- to 4-fold higher than that in bulk crystals. Furthermore, trap density decreased gradually toward the center of the crystal, and its distribution along the normal direction was not symmetric despite the contact between both surfaces of the thin single crystal with PTAA/ITO during growth.

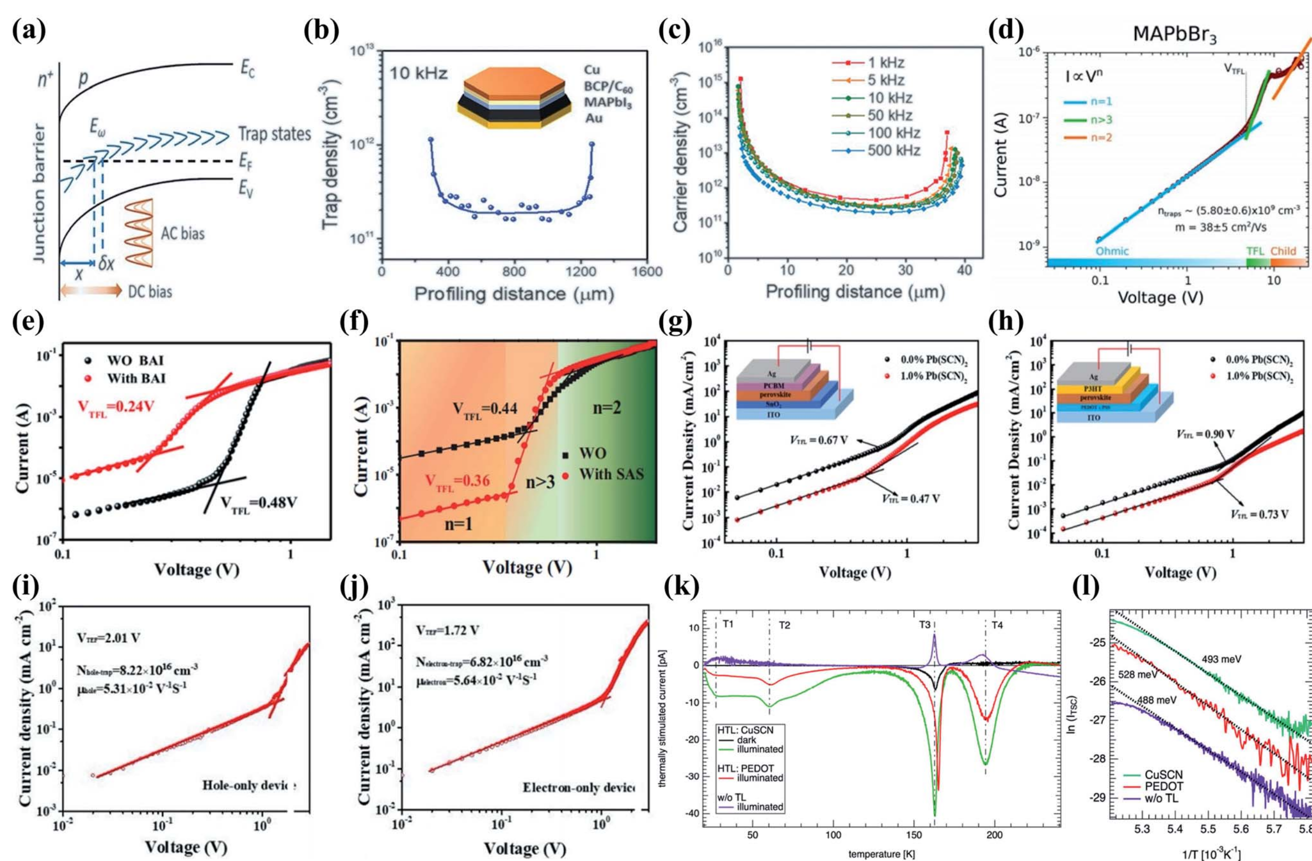

Fig. 4 (a) Schematic of band bending of a p-type semiconductor with deep trap states in an n^+–p junction. (b) Dependence of the trap density on the profiling distance of a $MAPbI_3$ single crystal measured by DLCP. (c) Spatial distributions of trap states in a $MAPbI_3$ thin single crystal, as measured by DLCP. Reproduced with permission:[36] copyright 2020, American Association for the Advancement of Science. (d) Characteristic *I*–*V* trace (purple markers) showing three different regimes for $MAPbBr_3$ (at 300 K). Reproduced with permission:[38] copyright 2015, American Association for the Advancement of Science. (e) Dark current–voltage curves of electron-only devices with the FTO/TiO_2/perovskite (BAI)/PCBM/Ag structure. Reproduced with permission:[96] copyright 2020, Wiley-VCH. (f) Dark current–voltage curves of the $CsPbIBr_2$ PSC devices with the FTO/TiO_2/perovskite/PCBM/Ag structure. Reproduced with permission:[97] copyright 2019, Wiley-VCH. Dark current–voltage curves from (g) electron-only and (h) hole-only devices based on 0.0% and 1.0% $Pb(SCN)_2$ with the structure shown in the inset. Reproduced with permission:[98] copyright 2019, Wiley-VCH. Current density–voltage characteristics of (i) hole- and (j) electron-only devices for estimating defect density in the 2D perovskite film. Reproduced with permission:[99] copyright 2020, American Chemical Society. (k) Thermally stimulated current for the devices with a CuSCN HTL (green), a PEDOT:PSS HTL (red), and without transport layers (purple). The dark TSC reference measurement for the ITO/CuSCN/MAPI/PCBM/C_{60}/Au configuration is also shown (black). (l) Arrhenius plots of the initial rise of the T4 TSC peak for the devices with a CuSCN HTL (green), a PEDOT:PSS HTL (red), and without transport layers (purple). Reproduced with permission:[102] copyright 2015, American Chemical Society.

Published on 14 giugno 2022. Downloaded on 16/07/2024 00:14:22.

2.1.3 Space-charge-limited-current (SCLC). The defects present in semiconductors could capture and trap free charges, thereby altering the electrical properties of materials after filling of the defects. Space-charge limited current (SCLC) has widely been utilized to measure properties associated with defects, including conductivity, carrier concentration, carrier mobility, and defect density.[37] In the SCLC method, the subjection of a semiconductor to a sufficiently large electric field through ohmic contacts would inject electric charges into the material to generate a current flow. The defect sites present will capture some of the injected charges, thereby reducing the density of free charges. Since the current is limited by the space-charge effect, the defect density in the semiconductor can be obtained from the curve of current *vs.* voltage (*I*–*V*) in the region of space-charge-injected current.[93]

The *I*–*V* curves are often plotted on a double logarithmic scale and analyzed according to SCLC theory. Fig. 4d shows a typical *I*–*V* curve of PSCs based on $MAPbBr_3$ single crystals divided into three regions:[38] the ohmic region, the trap-filled limit (TFL) region, and the Child region. At low voltages, the *I*–*V* curve (labeled in blue) can be linearly fitted to $I \propto V^{n=1}$ when defects are filled by some injected charges. After filling all defects by charges at a particular onset voltage, the injected charges will freely move through $MAPbBr_3$, leading to a rapid jump in current reaching the low resistance state at the onset voltage of the trap-filled limit (V_{TFL}). As a result, the defect (trap) density (n_{trap}) can be estimated according to eqn (5):[38]

$$N_t = \frac{2\varepsilon_0 \varepsilon_r V_{TFL}}{eL^2} \quad (5)$$

where L, ε_r, ε_o, and e are the thickness of the MHP film, dielectric constant of the material, permittivity of vacuum, and electronic charge, respectively.

For MHPs, the defects can either be hole-traps or electron-traps.

Recently, the SCLC method has not only been used to analyze the trap-state density and carrier mobility of MHP single crystals,[94,95] but also for defect passivation of PSCs. A better understanding of associated optoelectronic properties requires accurate characterization of trap density in MHPs. Hence, SCLC was employed in our work to explore the decrease in trap state density and restrained non-radiative recombination in all-inorganic $CsPbIBr_2$ PSCs by incorporating butylammonium iodide (BAI) (Fig. 4e). The trap densities of pristine and modified $CsPbIBr_2$ perovskite films were calculated to be 6.8×10^{15} and 3.4×10^{15} cm^{-3}, respectively.[96] Thus, BAI modification could reduce the trap state density to achieve superior crystallinity and morphology, conducive to better device performance. We also analyzed the trap-state density of pristine $CsPbIBr_2$ film and 0.7% sulfamic acid sodium salt (SAS)-incorporating $CsPbIBr_2$ film.[97] The calculated N_t of the $CsPbIBr_2$ film with and without SAS are 5.10×10^{15} and 6.24×10^{15} cm^{-3}, respectively (Fig. 4f). In region $n = 2$, the carrier mobilities of $CsPbIBr_2$ with and without additive were calculated to be 3.03×10^{-3} and 2.75×10^{-3} cm^2 V^{-1} s^{-1}, respectively. Therefore, effective defect passivation occurred in the bulk $CsPbIBr_2$ film by SAS. Ye *et al.* reported a $CsPbI_2Br$ film with 1.0% $Pb(SCN)_2$ with higher current density than that of the pristine film, indicating a smaller resistance and better charge transport properties.[98] Ye *et al.* also used SCLC (Fig. 4g and h) to investigate the influence of $Pb(SCN)_2$ on the trap states of $CsPbI_2Br$ films and final PSCs. Their data revealed a linear interrelationship between current and bias voltages at low bias voltages, while the current increased nonlinearly with voltage at higher bias voltages. Both the electron-only and hole-only devices with 1.0% $Pb(SCN)_2$ exhibited lower V_{TFL} values, implying significantly reduced electron trap densities by $Pb(SCN)_2$.

The SCLC method has also been applied to investigate different defect behaviors in 2D perovskites in comparison with 3D perovskites. In this respect, Liu *et al.* utilized SCLC measurements to gain a better understanding of the charge trap density and carrier mobility in 2D $BA_2MA_3Pb_4I_{13}$ perovskite films.[99] The current density–voltage (*J*–*V*) curves of electron-only and hole-only devices were used to calculate the hole and electron trap density in 2D perovskite films (Fig. 4i and j). Values of 8.22×10^{16} and 6.82×10^{16} cm^{-3} were obtained, which were significantly higher than those of previously reported 3D perovskite films (4.12×10^{15} cm^{-3} and 3.22×10^{15} cm^{-3}), respectively. Consequently, more severe carrier recombination may have occurred in 2D perovskite films. Besides, the fitted *J*–*V* curves at the SCLC region induced hole and electron mobility of approximately 5.31×10^{-2} and 5.64×10^{-2} cm^2 V^{-1} s^{-1}, respectively, for 2D perovskite films. These values were considerably lower than those of 3D perovskite films, indicating decreased carrier mobility and impediment of carrier transmission by introduction of long-chain butylamine as a spacer.

2.1.4 Thermally stimulated current (TSC). Thermally stimulated current (TSC) is a technology based on dielectric physics widely used to study trap energy level distribution and surface transport of carriers in MHPs.[100] To conduct TSC measurements, the device should first be cooled to a very low temperature, and carriers were then generated by illumination. Afterward, the device was kept at a constant temperature to allow carriers to relax the internal density state and occupy possible trap states. After the thermalization process, the temperature was raised slowly at a constant rate to release trapped electrons. The shallow-level trap was released at low temperatures, while the deep state carrier current was released at higher heat energy. The generated I_{TSC} was then detected to construct TSC curves. The trap density n_t on the material surface can be determined by relevant processing of TSC curves and calculations using eqn (6) and (7).[101]

$$I_{TSC} = \exp\left(-\frac{E_A}{k_B T}\right) \quad (6)$$

$$\int_{peak} I_{TSC} dt \le e n_t V \quad (7)$$

where E_A represents the activation energy, k_B is the Boltzmann constant, T refers to the temperature, e is the basic charge, and V denotes the sample volume.

Baumann *et al.* used TSC measurements to study the electron trap states of $MAPbI_3$ planar PSCs composed of ITO/poly(3,4-ethylenedioxythiophene):poly(styrenesulfonate)

 This journal is © The Royal Society of Chemistry 2022

Published on 14 giugno 2022. Downloaded on 16/07/2024 00:14:22.

(PEDOT:PSS)/$MAPbI_3$/PCBM/C_{60}/2,9-dimethyl-4,7-diphenyl-1,10-phenanthroline (BCP)/Au (red curve, Fig. 4k) and ITO/CuSCN/$MAPbI_3$/PCBM/C_{60}/BCP/Au (green curve, Fig. 4k).[102] For each device, the TSC trajectory was plotted as a function of temperature. The two peaks at very low temperatures (T_1 and T_2) were low-level defect traps in the PCBM/C_{60} electron transport layer owing to the absence of the electron transport layer. Also, the two low-temperature peaks vanished, indicating that most shallow traps must be located in the transport layer instead of the perovskite layer. The other two TSC peaks at higher temperatures were assigned to the perovskite layer. The first peak was attributed to the phase transition of the perovskite crystal around T_3 (163 K), and the second peak at around T_4 (194 K) was related to the charge trap analyzed using the initial ascent method. The activation energy of the trap state in $MAPbI_3$ perovskite films at T_4 was calculated according to eqn (6) and Arrhenius plots and the resulting value was about 508 ± 20 meV (Fig. 4l). The lower limit of defect density was calculated using eqn (7) to be 1×10^{21} m^{-3}.

2.1.5 Deep-level transient spectroscopy (DLTS). The release of charges captured by shallow-level defects could influence the electrical properties of semiconductors. Deep-level transient spectroscopy (DLTS) analysis has improved features related to sensitivity, range of observable defect depths, and facile operation.[103] Using DLTS, the emission rate window may easily be set and the instrument would only respond when a transient is detected with a rate within the set window. Thus, the variation of the emission rate of a defect in the set window at different temperatures would yield a response peak at each specific temperature. The main principle of DLTS consists of using the variation in defect emission rate *versus* temperature to determine the energy differences between defect states and one band edge, as well as capture the cross-section of the defects.[104]

In typical DLTS, the capacitance transients are investigated by measuring the variations in capacitance as a function of temperature, usually in the range from liquid nitrogen temperature to room temperature (300 K) or above. During the initial bias pulse at low temperatures, defects could be filled by bias-generated charges. During this process, the capture rate of a defect trap should be much larger than its emission rate, making the latter negligible. The increase in temperature will yield DLTS peaks if the emission rate of a charge trapped by defects is within the set rate window. Hence, the defect density can directly be obtained from the capacitance change corresponding to the complete filling of the defect traps with a saturated injection pulse or the largest possible majority-carrier pulse. The defect density at a certain temperature can be described by eqn (8):[103]

$$n_{\mathrm{trap}} = 2(\Delta C/C)(N_{\mathrm{A}} - N_{\mathrm{D}}) \tag{8}$$

where ΔC and C are the capacitance change from $t = 0$ and the capacitance of the diode under quiescent reverse-biased conditions, respectively. $N_{\mathrm{A}} - N_{\mathrm{D}}$ represents the net acceptor concentration on the p side of the junction.

The E_{A} of the defects below the conduction band can be obtained according to eqn (9):[103]

$$e_n = (\sigma_n \langle v_n \rangle N_{\mathrm{D}}/g_n)\exp\left(-\frac{E_{\mathrm{A}}}{k_{\mathrm{B}}T}\right) \tag{9}$$

where e_n, σ_n, v_n, N_{D}, and g_n are the thermal emission rate of trapped charges, charge capture cross-section, mean thermal velocity of charges, effective density of states in the carrier band, and degeneracy of defects, respectively.

To distinguish the nature of defects (electronic or ionic) in $MAPbI_3$ perovskites, Reichert *et al.* applied reversed DLTS, meaning voltage change from 1 V to 0 V.[39] Other parameters, such as AC frequency and filling-pulse, remained constant. Unlike conventional DLTS measurements, the capture charge carriers' process in trap states was measured because of electronic traps. Since the emission rate was much lower than the capture rate, the latter (determined by reverse DLTS) was higher than the emission rate (obtained by conventional DLTS) when deep-level trap states were measured. The situation was different when mobile ions responded to voltage pulses. In the absence of applied external voltage, mobile ions were in an equilibrium state at the interfaces of perovskite layers due to the internal field. As a result, mobile ions were pushed into the perovskite layer by a voltage pulse. For ions, this process would be approximately as fast as the back drift of ions to the interfaces. The measured reverse DLTS at room temperature and the plot of boxcar evaluation at a rate window of $t_2/t_1 = 2$ are provided in Fig. 5a. The emission rates of all defects looked comparable for the conventional and reverse DLTS. Hence, the measured emission rates originated from mobile ions instead of charge carriers, such as electrons and holes. After conducting DLTS tests of PSCs following algorithm analyses, three different types of mobile ions corresponding to different examples of defect parameters were recorded. Notably, the strong capacitance freeze-out presented a serious obstacle for DLTS measurements. Here, the dominant feature consisted of a very prominent peak near 150–200 K related to the rapid increase in capacitance as a function of temperature. This produced a false peak, not associated with a deep level trap as clearly shown by the independence of the peak position of the time window. However, the signal of real traps became considerably distorted by the false peak arising from capacitance freeze-out. To eliminate this effect and obtain clean spectra, Polyakov *et al.* corrected the signal by a known rate of change with temperature of the steady-state capacitance in DLTS of $MAPbI_3$ perovskites.[105] The corrected DLTS signal (Fig. 5b) showed two features at high temperatures (>200 K). The first was related to a hole trap (negative peak A according to convention in Fig. 5b, that is the capacitance decreases with time during the transient) while the other was linked to electron traps (positive peak B). Unlike false peaks, such peak positions moved as a function of the time window, thereby belonging to real traps. The slight temperature dependence of the electron trap peak B intensity resulted from interference with the hole trap peak A, while the stronger temperature dependence of the hole trap peak A intensity issued from the temperature dependence of free electron concentration. The hole trap displayed an activation energy of 0.57 eV and a capture cross-section of 4.2×10^{17} cm^2, whereas the corresponding values of the electron trap were around 0.74

Published on 14 giugno 2022. Downloaded on 16/07/2024 00:14:22.

eV and 2.7×10^{16} cm^2, respectively. The energies of such trap levels agreed reasonably with state-of-the-art density functional calculations that predicted the existence of interstitial iodine defects at energies of 0.57 eV and 0.8–0.9 eV of the conduction band for the first two levels.

2.2 Spectrometric characterization

Carrier dynamics is the key issue when studying the performance of semiconductor devices. Efficient carrier transport refers to the transfer of electrons and holes from one monomer to another without being dispersed or captured by traps. Carrier mobility can indirectly provide useful defect information. In this section, we briefly review the methods for measuring carrier mobility in PSCs, including steady-state PL emission (ssPL), transient absorption (TA) spectroscopy, photo-induced charge extraction with linearly increasing voltage (photo-CELIV), time-resolved microwave conduction (TRMC) method and time-resolved Kerr rotation (TRKR) measurement.

2.2.1 Steady-state PL emission (ssPL). In steady-state PL emission (ssPL) measurements under ambient conditions, MHP films become photo-excited with the increase in pump fluence, thereby exhibiting correlated photoemission properties. After photo-excitation, the excited-state carriers in MHP films are emitted through band gap relaxation or trapped by defect traps. The turning point of low pump fluence represents photo-generated charge required to fill all defect traps, meaning the threshold trap pump fluence $P_{\text{th}}^{\text{trap}}$. The total defect density n_{trap} (bulk and surface) can be estimated following eqn (10):[106]

$$n_{\text{trap}} = P_{\text{th}}^{\text{trap}} \times \frac{\alpha}{E} \tag{10}$$

where α and E represent the absorption coefficient and energy of a photon at the laser pulse wavelength, respectively.

At low pump fluence, the Auger recombination is negligible, and defect-mediated charge recombination should be much slower than the band-edge radiative recombination. The bulk/surface corresponding defect density of states can be calculated using relevant kinetic equations.

Xing *et al.* used ssPL to reveal the existence of two types of traps in $MAPbI_3$ films (Fig. 5c and d).[107] The bulk density of defect states was estimated to be 5×10^{16} cm^{-3}, while the density of defect states on the surface was about 1.6×10^{17} cm^{-3}. Yuan *et al.* employed ssPL spectroscopy to compare the defect state densities of $MAPbI_3$ and $FAPbI_3$ films as a function of pump fluence.[40] As shown in the inset of Fig. 5e, the first intersection representing the pump energy required filling all the traps, meaning the threshold trap pump energy (about 1 μJ cm^{-2}) corresponding to a trap state density of about 10^{17} cm^{-3}. In contrast, the $MAPbI_3$ film had a higher threshold (about 6 μJ cm^{-2}) than the $FAPbI_3$ film, indicating an elevated density of trap states (about 2.5×10^{17} cm^{-3}) (Fig. 5f).

2.2.2 Transient absorption (TA) spectroscopy. Transient absorption (TA) spectroscopy, also known as pump–probe

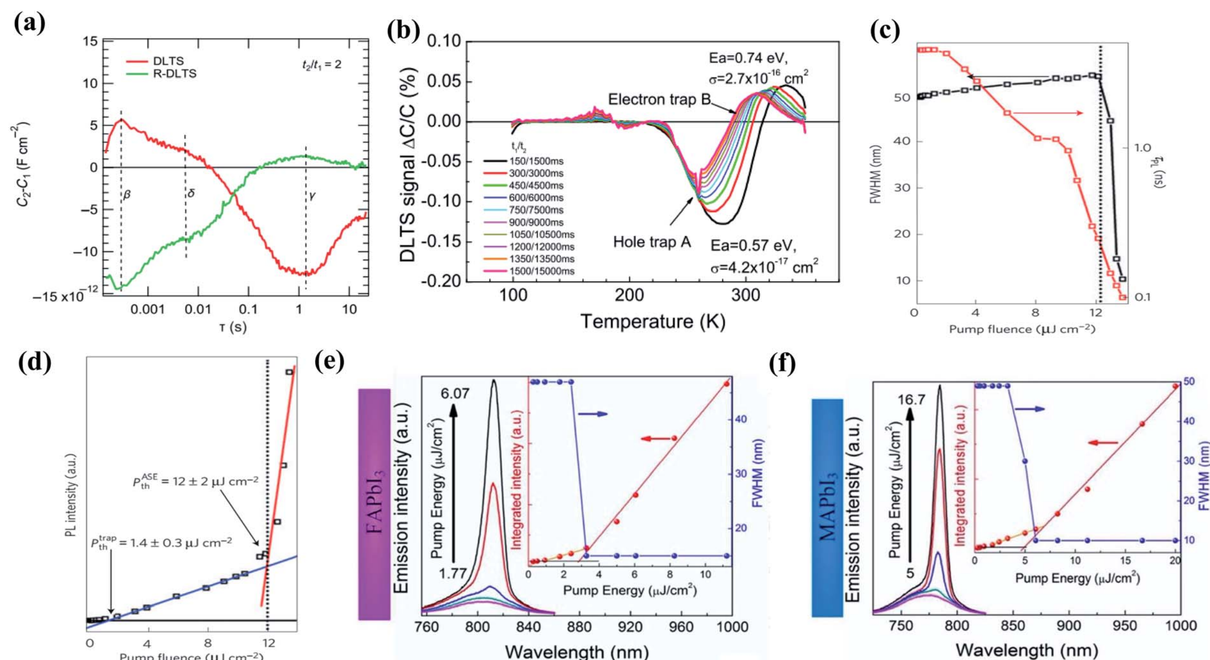

Fig. 5 (a) Conventional DLTS and reverse DLTS evaluation *via* boxcar at room temperature with a rate window of $t_2/t_1 = 2$. Reproduced with permission:[39] copyright 2020, American Physical Society. (b) DLTS spectra as corrected for the strong capacitance freeze-out, and various time windows t_1 and t_2. Reproduced with permission:[105] copyright 2018, AIP Publishing. (c) FWHM of the emission peak and average transient PL lifetime (τ_{PL}) as a function of the pump fluence. τ_{PL} is the time taken for the intensity to decrease to 1/*e* of its initial value. (d) PL intensity as a function of pump fluence. The dashed vertical black lines in (c) and (d) indicate the onset of ASE. Reproduced with permission:[107] copyright 2014, Nature Publishing Group. (e) Face emission spectra of $FAPbI_3$ film pumped by a pulsed laser with a duration of 150 fs. (f) Face emission spectra of $MAPbI_3$ film pumped by a fs pulsed laser. The insets show the integrated emission intensity and the FWHM of the face emission spectra as a function of pump energy. Reproduced with permission:[40] copyright 2017, American Chemical Society.

 This journal is © The Royal Society of Chemistry 2022

Published on 14 giugno 2022. Downloaded on 16/07/2024 00:14:22.

technology, was first applied in the field of photochemistry. Nowadays, TA measurements are used to study the energy transfer and charge transfer processes in semiconductors after light absorption.[76,108] Hence, TA might be employed for further design of PSCs and improve the performance of devices. In TA, small amounts of samples are excited by high-energy pump light to release energy instantaneously and excite the sample from the ground state to the excited state. Next, the same point of the sample is irradiated with another weak broadband white light (probe light). The intensities of the probe light and reference light after passing through the sample can be measured with a high precision detector (CMOS/NMOS) by adjusting the time delay between the pump light and probe light with an optical delay line. The differential absorption spectrum of the sample can be obtained by recording the detection light and reference light intensities of the sample with and without pump light by controlling the passage and occlusion of the pump light with a chopper. In general, the change in absorption ΔA of a sample can be calculated using eqn (11):

$$\Delta A(\lambda) = -\log\{[I(\lambda)_{\text{pro}}/I(\lambda)_{\text{ref}}]_{\text{pump}}/[I(\lambda)_{\text{pro}}/I(\lambda)_{\text{ref}}]_{\text{unpump}}\} \quad (11)$$

where $\Delta A(\lambda)$ represents the change in absorption as a function of detection wavelength, I is the light intensity measured by the detector, $[I(\lambda)_{\text{pro}}/I(\lambda)_{\text{ref}}]_{\text{pump}}$ refers to the ratio of light intensities of the probe light and reference light when the pump light passes through the sample, and $[I(\lambda)_{\text{pro}}/I(\lambda)_{\text{ref}}]_{\text{unpump}}$ denotes the ratio of the intensity of the probe light to the reference light when the pump light is blocked.

The carrier relaxation process of a sample can be analyzed using a linear stage to adjust the time delay of the probe light reaching the sample surface relative to the pump light, as well as record changes in probe light absorption spectroscopy under continuous-time delay. However, unlike steady-state absorption spectroscopy, the $\Delta A(\lambda)$ of the transient absorption spectrum contains positive (+) and negative (−) signals, where the signal may change from positive to negative or *vice versa*. For example, the signals of molecular systems usually originate from contributing excited state absorption (ESA) signals, ground state bleaching (GSB) signals and stimulated emission (SE)

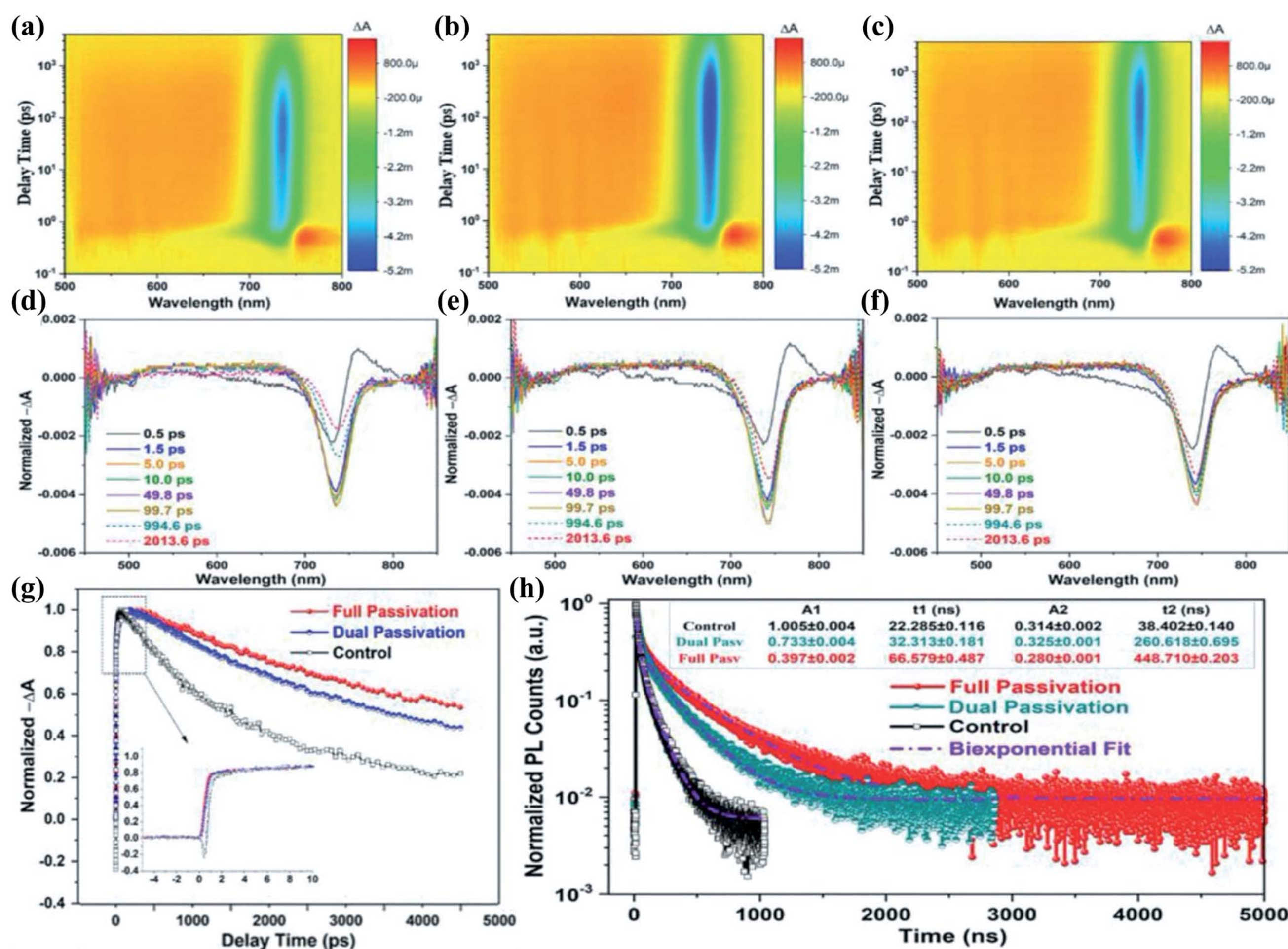

Fig. 6 The pseudocolor TA plots for (a) the control perovskite film and the perovskite films with (b) dual defect passivation and (c) full defect passivation. TA spectra showing the PB1, PB2, and PA signatures at various probe delays for perovskite films (d) without CAS-Cl passivation, (e) with dual defect passivation, and (f) with full defect passivation. (g) 400 nm pumped TA kinetics probed at the PB2 peak and (h) biexponential function fitted TrPL spectra for the perovskite films. Reproduced with permission:[75] copyright 2020, Wiley-VCH GmbH.

Published on 14 giugno 2022. Downloaded on 16/07/2024 00:14:22.

signals. Liu *et al.* used the TA measurement method to reveal the excellent carrier dynamics of a perovskite layer with complete defect passivation.[75] A sharp photo-bleaching (PB) signal band carrier decay was observed in the band edge of CsFAMA perovskites in accordance with the dominant band-to-band carrier recombination (Fig. 6a–c). Two negative ΔA valleys were detected at approximately 480 nm (PB1) and 760 nm (PB2), caused by the combination of PB and SE signals (Fig. 6d–f). Note that the generation, decay, and recombination of carriers in perovskites mainly depend on the PB signal in the band-edge region. In the initial stage from 0 to 5 ps, the changes in PB2 peaks of perovskite samples were independent of the introduced cysteamine hydrochloride (CAS-Cl) since 3D perovskites generally possess Wannier–Mott type excitons due to the low exciton binding energy ($\approx$12 meV). The PB2 peak of pristine perovskites started to vanish at 994.6 ps after excitation to become almost quenched at 2013.6 ps. By comparison, the PB2 peak of double-defect passivation or full-defect passivation perovskites stabilized for a longer time, confirming the longer lifetime of defect-passivated perovskite films (Fig. 6g). Meanwhile, the carrier lifetime of perovskite films increased after double passivation or full passivation (Fig. 6h).

Li *et al.* used femtosecond TA measurements to confirm the enhanced phase purity and suppressed nonradiative recombination in quasi-2D perovskite films.[109] Fig. 7a and d show two signals: negative (blue) GSB and positive (yellow) ESA. For the pristine quasi-2D $CsPbI_3$ film, the positive band at $\approx$500 nm in the short wavelength region belongs to the low-dimensional phase ESA, while it is not obvious in the optimized film, indicating that the *N*-methyl-2-pyrrolidone iodide (NMPI) additive

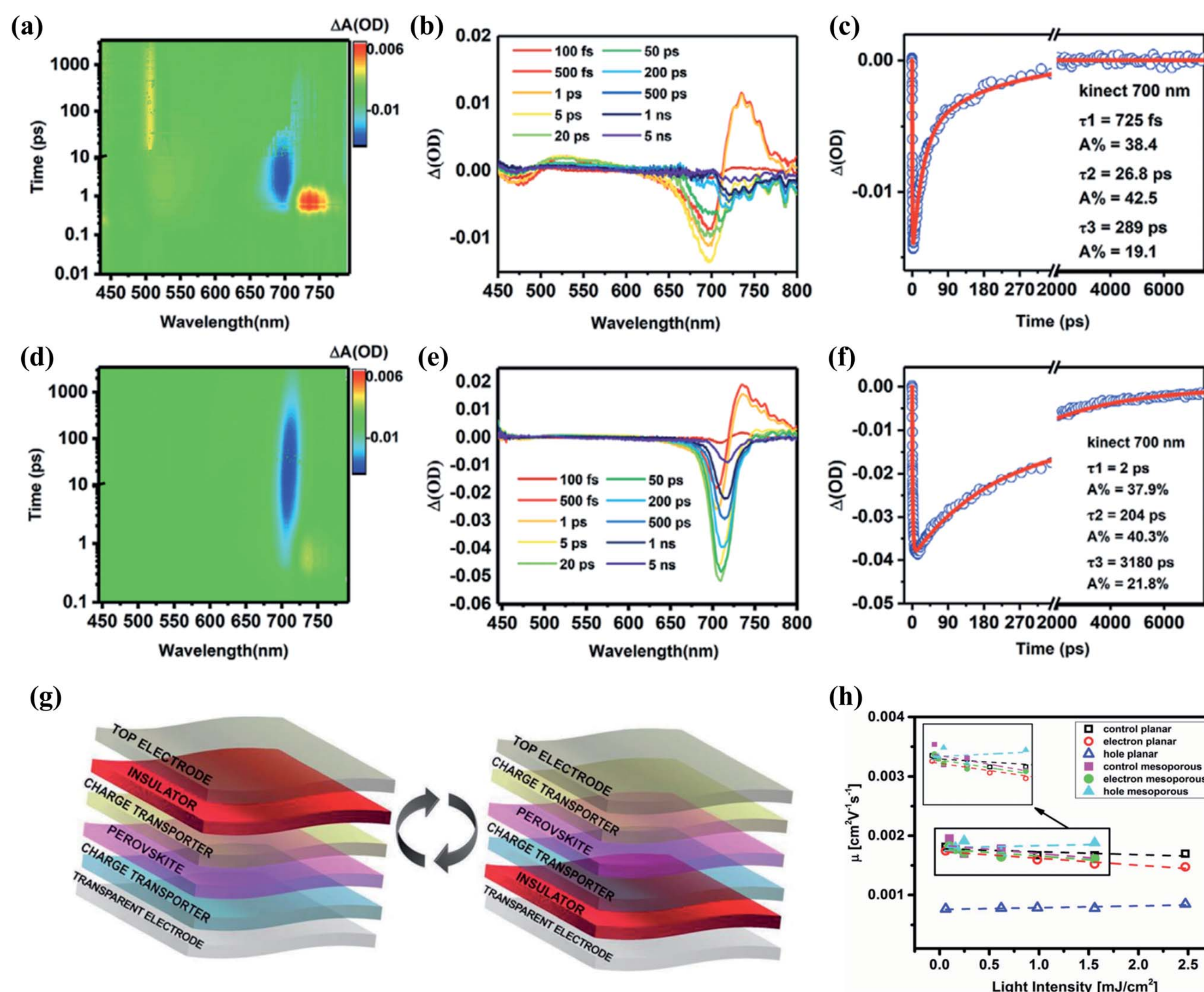

Fig. 7 TA spectra obtained following a 400 nm laser pulse excitation of the (a–c) pristine (0% NMPI) and (d–f) optimized (2% NMPI) quasi-2D (n = 20) $CsPbI_3$ films: (a and d) Time- and wavelength-dependent 3D plot TA images; (b and e) TA spectra at selected probe times; (c and f) the TA kinetics curves. Reproduced with permission:[109] copyright 2021, Wiley-VCH GmbH. (g) Implementation of the insulating layer into the solar cell structure for charge selective photo-CELIV. (h) Correlation between charge carrier mobility and photogenerated light intensity governed by the applied laser pulse, for control and charge selective samples after a 7 μs pulse delay. Reproduced with permission:[114] copyright 2017, Wiley-VCH Verlag GmbH & Co. KGaA, Weinheim.

 This journal is © The Royal Society of Chemistry 2022

Published on 14 giugno 2022. Downloaded on 16/07/2024 00:14:22.

can improve the phase purity. TA spectra at different time scales of charge carrier dynamics are shown in Fig. 7b and e. After 5 ns, the bleaching signal of the pristine quasi-2D $CsPbI_3$ film decays almost completely, while the optimal bleaching signal shows a clear signal, indicating a longer decay time for carriers after the introduction of NMPI additive. Furthermore, the TA kinetics of the pristine and optimized quasi-2D ($n = 20$) $CsPbI_3$ films (Fig. 7c and f) show that the carrier extraction time of the pristine quasi-2D $CsPbI_3$ film (725 fs to 26.8 ps) is shorter than that of the optimized film (2–204 ps), but the τ_3 of the latter is 10 times longer than that of the pristine film (3180 *vs.* 289 ps). The prolonged τ_3 suggests that the NMPI additive optimized the crystallization kinetics of quasi-2D $CsPbI_3$, improved the morphology and phase purity, and thereby enhanced the carrier lifetime and reduced the trap density.

2.2.3 Photo-induced charge extraction by linearly increasing voltage (photo-CELIV). The photo-CELIV technique characterizes defects by testing the carrier mobility to confirm the passivation effect. Following the pioneering work of Juska *et al.*, photo-CELIV has been widely used to study charge transport in organic semiconductor films.[110,111] In photo-CELIV measurements, charge carriers are photogenerated in semiconductor layers. Subsequently, photo-induced carriers are extracted by applying a linear voltage pulse (reverse bias), and the corresponding transient extraction current can be obtained from eqn (12):[112]

$$j(t) = j_0 + \Delta j(t) \tag{12}$$

In eqn (12), Δj is the average conduction current of mobile charge carriers within the active layer. $j_0 = CA$ is the average displacement current, where C is the geometric capacitance of the active layer and A is the voltage rise rate. Feature extraction time t_{max} is observed when a linearly increasing voltage is applied to a sample with blocked contacts. Under the condition of $\Delta j \leq j_0$, the mobility μ is given by eqn (13):[113]

$$\mu = \frac{2d^2}{3At_{max}^2} \tag{13}$$

where d is the sample thickness, A is the applied voltage gradient and t_{max} is the maximum carrier extraction time. By integrating the CELIV transients, the equilibrium and photogenerated carrier densities can be obtained in the dark and in the light, respectively. By varying the delay time between excitation and voltage sweep, excited carrier dynamics on the microsecond timescale can also be obtained, which can reveal relevant information about carrier recombination within the device.

Petrović *et al.* explored the charge carrier mobility and transport properties of mesoporous and inverted planar-structured PSCs by the photo-CELIV technique (Fig. 7g).[114] It was found that highly balanced charge mobilities were obtained in mesoporous devices, whereas in planar devices, the hole mobility was a half order of magnitude lower than the electron mobility due to the inferior hole injection ability from poly(3,4-ethyledioxthiophene) polystyrene sulfonate (PEDOT:PSS) to the spiro-OMeTAD interlayer (Fig. 7h). Furthermore, dispersive transport is found in electron-selective devices with TiO_2 ETLs, which indicates the presence of a considerable number of trapped states at the perovskite interface, whereas the planar devices do not have these trapped states. Chen *et al.* determined the hole and electron mobilities of $CH_3NH_3PbI_3$ perovskites by the photo-CELIV technique and revealed the recombination process and trap states. The results show that efficient and balanced transport is achieved in both $CH_3NH_3PbI_3$ pure films and $CH_3NH_3PbI_3$/phenyl-C61-butyric acid methyl ester (PC61BM) bilayer solar cells.[115] Furthermore, the charge mobility of the pure $CH_3NH_3PbI_3$ film was 3.2×10^{-4} cm^2 V^{-1} s^{-1}, which is almost doubled to 7.1×10^{-4} cm^2 V^{-1} s^{-1} upon insertion of the PC61BM layer (Fig. 8a and b).

2.2.4 Time-resolved microwave conductivity (TRMC). Time-resolved microwave conductivity (TRMC) can be used to study the electronic properties and carrier dynamics of Cl-doped MHPs. Xu *et al.* observed a 2-fold increase in both carrier mobility and lifetime (Fig. 8c and d).[116] To reduce surface recombination, a LiF passivation layer was fabricated on a perovskite surface. According to TRMC, perovskites with and without a LiF passivation layer showed the same mobility and lifetime, suggesting enhanced photocarrier transport in MHPs mainly determined by bulk properties instead of the nature of the surface. Meanwhile, dark microwave conductivity measurements showed a 2-fold decrease in dark carrier density (from 7.8×10^{15} cm^{-3} to 2.9×10^{15} cm^{-3}), confirming declined defect density in MHPs (Fig. 8e). Oga *et al.* examined the local charge carrier mobility and recombination kinetics in $CH_3NH_3PbI_3$ perovskites deposited on mp-TiO_2 and mp-Al_2O_3 substrates by the TRMC method.[117] They noticed a close relationship between the local charge carrier mobility and recombination kinetics with the crystal composition of perovskites and residual PbI_2 after conversion to perovskites. Simultaneously, the changes in complex transient conductivities with excitation laser power and microwave frequency displayed extremely high carrier mobilities and low trap densities of the perovskites on mp-TiO_2 substrates.

2.2.5 Time-resolved Faraday rotation (TRFR) measurement and time-resolved Kerr rotation (TRKR) measurement. Both time-resolved Faraday rotation (TRFR) and time-resolved Kerr rotation (TRKR) measurements are performed using optical pump–probe techniques with remarkable sensitivity to the transient filling of spin sub-levels of electrons and holes. Hence, they are mainly used for probing information about the spin dynamics of charge carriers in materials.[118,119] TRFR and TRKR techniques involve two ultra-short laser pulses. The first consists of a circularly polarized pump laser pulse and the second involves a linearly polarized probe pulse. When the circularly polarized pump pulse reaches the sample, a macroscopic spin polarization will be established. The contact between the linearly polarized probe pulse (with a time delay of Δt from the pump pulse) and the sample characterized by an established spin polarization will influence the refractive index n of the probe pulse. The spin dynamics information of the carriers can be obtained by the evolution process of the probe pulse as a function of delay time. TRFR detects the deflection angle θ_F of transmitted light to yield spin evolution of

polarization *versus* delay time. TRKR obtains the evolution process of spin polarization in samples *versus* delay time by detecting the deflection angle θ_K of reflected light, suitable for nontransparent samples.

Giovanni *et al.* studied the spin dynamics of $CH_3NH_3PbI_3$ by TRFR measurements and recorded lifetimes $\tau_1 = 0.9 \pm 0.1$ ps (holes) and $\tau_2 = 4 \pm 1$ ps (electrons), consistent with the values measured for intraband angular momentum flip ($\tau_h = \sim 1.1$ ps for holes and $\tau_e = \sim 7$ ps for electrons) (Fig. 8f and g).[120] The degree of light-induced Faraday rotation reached as high as 720 milli-degrees for $CH_3NH_3PbI_3$ polycrystalline thin films (or 10° $\mu m^{-1} \pm 2° \mu m^{-1}$) with a thickness of approximately 70 nm at 200 K. Liu *et al.* further confirmed the decline in defect densities of perovskite films by detecting the longitudinal spin relaxation time by TRKR spectroscopy.[121] The spin relaxation process in perovskite crystals was found to be dominated by the scattering mechanism based on Elliott–Yafet (EY). The TRKR results revealed an increase in spin lifetime from 10 ps to 31 ps as temperature decreased from 120 K to 14 K (Fig. 8h). Compared to other reports, the spin relaxation time rose by 2-fold, further demonstrating the excellent quality of the crystal film.

2.3 Microscopy characterization

2.3.1 Kelvin probe force microscopy (KPFM). Kelvin probe force microscopy (KPFM) is a surface potential measurement technique based on atomic force microscopy (AFM). By measuring the contact potential difference (CPD) between the probe tip and surface of the sample, the potential distribution on various flat materials can be drawn at the sub-nanometer resolution.[122,123] Meanwhile, the nanoscale electrical properties can be analyzed to realize quantitative measurements of local potential and their distributions. KPFM as a non-destructive testing method has a wide range of applications in the research of metal nanostructures, semiconductor materials, and electronic devices.

In high-resolution KPFM, CPD is greatly affected by the short distance force between the needle tip and sample. This can be defined by eqn (14):

$$V_{CPD} = \frac{\Phi_t - \Phi_s}{-e} \tag{14}$$

where Φ_t and Φ_s are respectively the work functions of the sample surface and needle tip surface, while e is the electric charge.[124]

In KPFM, the sample surface morphology characteristics are first drawn by AFM and the height of the probe is then fixed to obtain the V_{CPD} data of the sample surface. KPFM measures the sample electrostatic force by electrically driving the cantilever with an applied drive voltage (V_{AC}) and bias voltage (V_{DC}). The

Published on 14 giugno 2022. Downloaded on 16/07/2024 00:14:22.

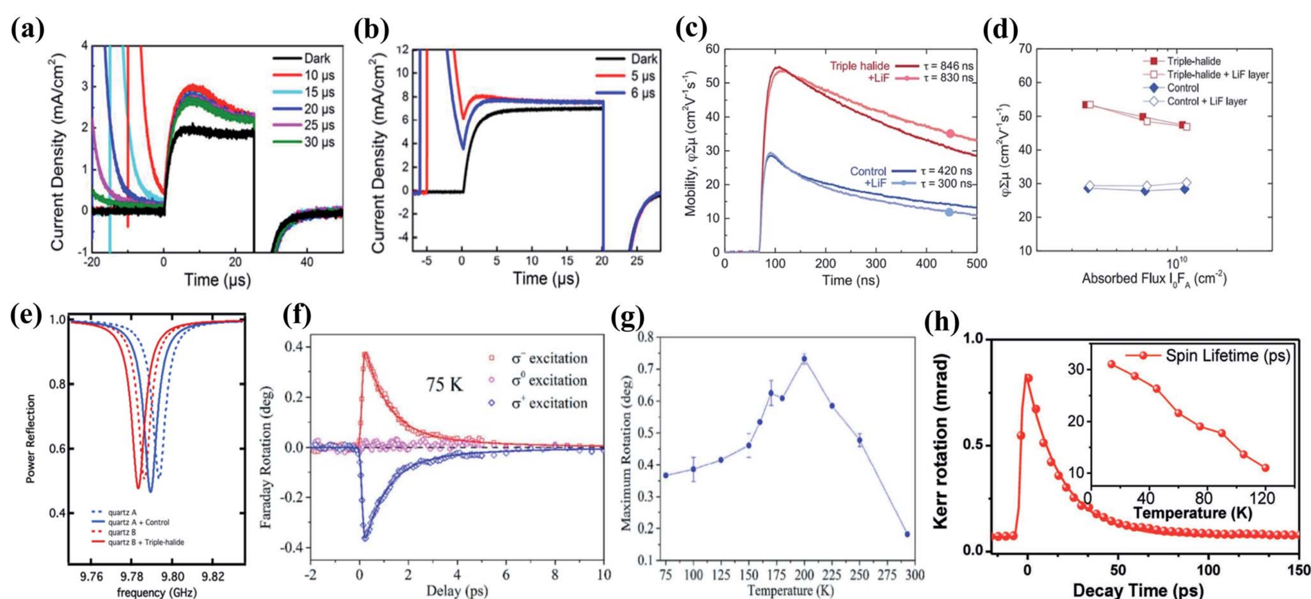

Fig. 8 Photo-CELIV *j*–*t* profiles with different delay times of (a) $CH_3NH_3PbI_3$ neat film at a voltage ramp of 2×10^4 V s^{-1} and (b) $CH_3NH_3PbI_3$/PC61BM bilayer cell at a voltage ramp of 1×10^5 V s^{-1}. Reproduced with permission:[115] copyright 2015, American Chemical Society. (c) Photoconductivity transient (indicative of the lifetime) measured by time-resolved microwave conductivity (TRMC), indicating double charge-carrier lifetime (*t*) in the 1.67 eV triple-halide film (Cs22Br15 + Cl3, red line) compared with the control film (Cs25Br20, blue line). (d) Photoconductivity under different excitation intensities. (e) Dark microwave conductivity (DMC) measurements of control (blue) and triple-halide (red) films on quartz substrates. Power reflection coefficient *versus* microwave frequency resonances is shown from the DMC measurements. Reproduced with permission:[116] copyright 2020, American Association for the Advancement of Science. (f) TRFR study on $CH_3NH_3PbI_3$ at a fluence of 19 μJ cm^{-2}. Typical signal of pump-induced Faraday rotation which is proportional to sample magnetization, fitted with a bi-exponential decay function ($\tau_1 = 0.9 \pm 0.1$ ps and $\tau_2 = 4 \pm 1$ ps). (g) Maximum rotation (peak) as a function of temperature. Reproduced with permission:[120] copyright 2015, American Chemical Society. (h) Time-resolved spin relaxation time for MA/EtOH-based perovskite films. The inset shows the spin lifetime as a function of temperature. Reproduced with permission:[121] copyright 2017 Wiley-VCH Verlag GmbH & Co. KGaA, Weinheim.

 This journal is © The Royal Society of Chemistry 2022

Published on 14 giugno 2022. Downloaded on 16/07/2024 00:14:22.

electrostatic force $F_{el}(Z)$ between the tip of the probe and the sample can be expressed by eqn (15):[125]

$$F_{el}(Z) = -\frac{1}{2}(V_{tip} \pm V_{CPD})^2 \frac{\partial C(Z)}{\partial Z} \tag{15}$$

where the sign (±) depends on the bias V_{DC} applied to the sample (+) or the probe (−), V_{tip} is the tip surface potential, and $C(Z)$ represents the tip surface capacitance.

The substitution of $V_{tip} = V_{AC}\sin(\omega t) + V_{DC}$ (where ω is the angular frequency of the applied driving AC voltage and t is the time) in eqn (16) would yield the electrostatic force.

$$F_{el}(Z,t) = -\frac{1}{2}\frac{\partial C(Z)}{\partial Z}[V_{DC} \pm V_{CPD} + V_{AC}\sin(\omega t)]^2 \tag{16}$$

This equation can be divided into three parts:

$$F_{DC} = -\frac{\partial C(Z)}{\partial Z}\left[\frac{1}{2}(V_{DC} \pm V_{CPD})\right]^2 \tag{17}$$

$$F_{\omega} = -\frac{\partial C(Z)}{\partial Z}(V_{DC} \pm V_{CPD})V_{AC}\sin(\omega t) \tag{18}$$

$$F_{2\omega} = \frac{1}{4}\frac{\partial C(Z)}{\partial Z}V_{AC}{}^2[\cos(2\omega t) - 1] \tag{19}$$

where F_{DC} represents the constant electrostatic force. F_{ω} and $F_{2\omega}$ are the electrostatic force of single frequency and double frequency AC phases, respectively. F_{DC} is used for measuring the topography signal, F_{ω} for measuring the CPD signal, and $F_{2\omega}$ for measuring the capacitance signal.

KPFM first generates static power by adding V_{DC} and V_{AC} to the probe and then uses a phase-locked amplifier to measure V_{CPD} and extract the frequency ω component. Here, the output signal is proportional to the difference between V_{CPD} and V_{DC}, where the V_{CPD} value is measured by applying V_{DC} to the AFM tip or sample. When V_{DC} equals V_{CPD}, the feedback is used to cancel the V_{CPD} by adjusting the constant component V_{DC} of the tip bias, thereby making the output signal of the phase-locked

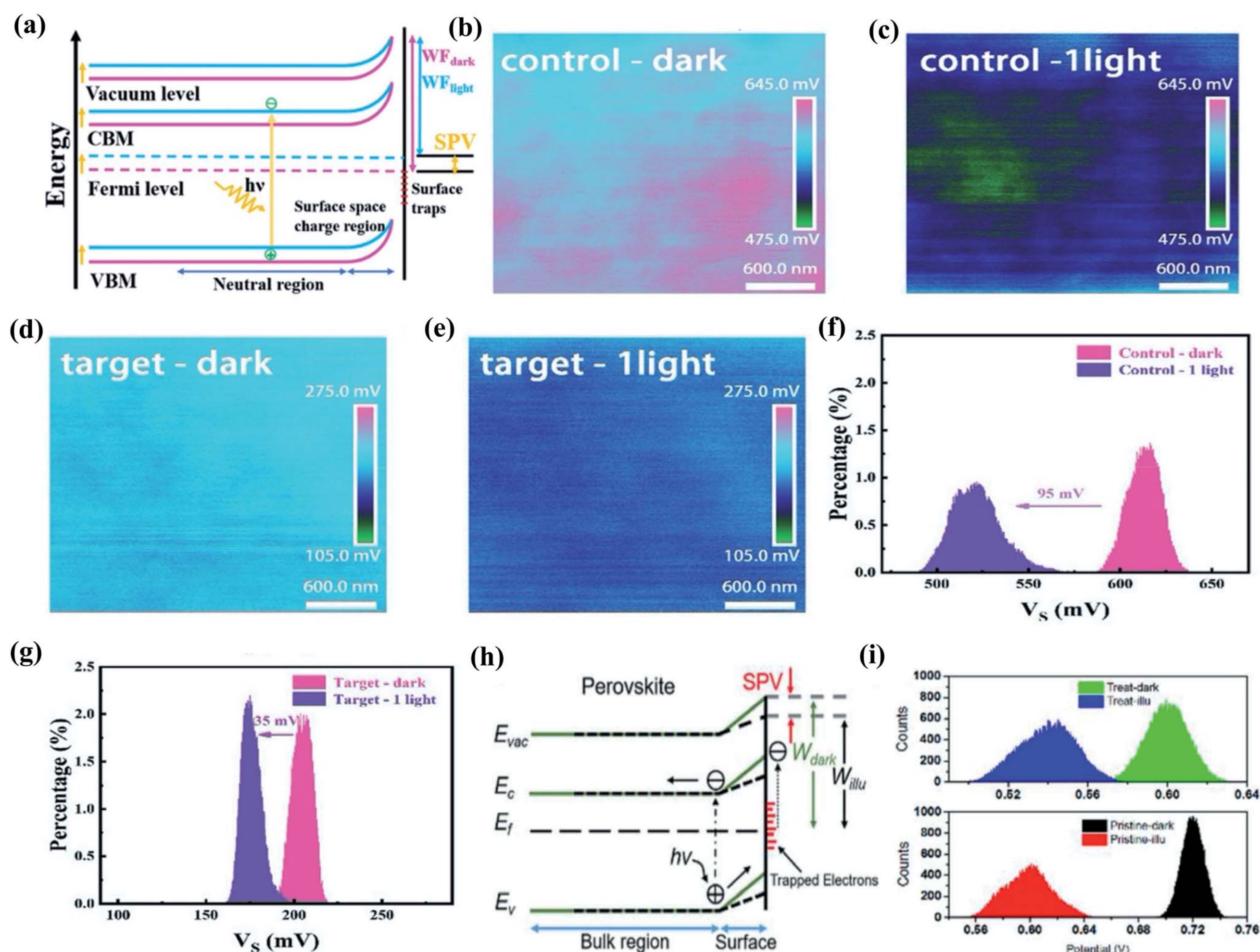

Fig. 9 KPFM measurement. (a) Schematic energy band diagram for SPV; surface potential differences of $CsPbI_3$ films without and with the improved intermediate process in the dark (b and d) or under light irradiation (c and e). SPD distribution and SPV of (f) the control and (g) the target $CsPbI_3$ films. Reproduced with permission:[126] copyright 2021, Wiley-VCH GmbH. (h) Schematic band diagram for the surface photovoltage (SPV) measurement at the perovskite surface. (i) Representative V_{CPD} potential histograms showing a change in the dark and under illumination. Reproduced with permission:[127] copyright 2017, American Chemical Society.

Published on 14 giugno 2022. Downloaded on 16/07/2024 00:14:22.

amplifier invalid and electrostatic force F_{ω} is equal to zero. This allows the V_{DC} value of each point on the sample surface to be obtained for drawing a potential map of the entire sample surface.

Tan *et al.* utilized KPFM to examine the surface defect passivation of $CsPbI_3$ perovskite films by measuring the contact potential difference (SPD) under dark or light conditions.[126] The changes in SPD between dark and light conditions, which can be defined as surface photovoltage (SPV) reflect the surface defect density of the sample. Under illumination, the presence of more defects on the film surface led to trapping of more photogenerated carriers, resulting in more obvious band bending on the film surface and larger variations in SPD (Fig. 9a). The smaller changes in the dark–light of the SPD of samples containing NH_4I, as well as the decrease in SPV from 75 mV to 27 mV, confirmed the effectively reduced electron trap state density near the surface of the perovskite film by NH_4I, inhibiting the recombination of trapped electrons and free holes (Fig. 9b–g). The V_{CPD} of $CsPbI_3$ perovskites with NH_4I declined from −355 to −423 mV. Also, the surface carrier concentration increases from 6.73×10^{13} to 9.67×10^{14} cm^{-3}. Therefore, the introduction of NH_4I diminished the surface trap state density and high surface carrier concentration. Li *et al.* used KPFM to further characterize the photophysical properties of perovskite films treated with and without chlorobenzene.[127] Under dark and light conditions, the surface of perovskite film accumulates carriers due to the existence of the trap state, resulting in surface band bending (Fig. 9h). Compared to untreated perovskite films, treated perovskite films with relatively low magnitude SPV suggested declined densities of trap states by chlorobenzene treatment, resulting in less non-radiative recombination and better photoelectric performance (Fig. 9i).

2.3.2 Scanning tunneling microscopy (STM) combined with density functional theory (DFT). Scanning tunneling microscopy (STM) can be combined with suitable density functional theory (DFT) calculations to investigate surface and sub-surface structures of MHPs. The examination of the electronic structure and morphology of MHPs with an unprecedented high resolution at the atomic level may provide a better understanding of interfacial properties.[128,129]

Ohmann *et al.* observed dislocations and defects in MHPs, where two Br atoms were found close together and oriented perpendicularly with respect to the main Br pair alignment.[130] Such rotation progressed diagonally at 45° to the main axis throughout the whole surface. The immediate neighboring pairs were also affected and oriented slightly off-line (see white lines in Fig. 10a), resulting in local ion arrangements displaying a chiral pattern. As a result, dislocation lines formed as a single or multiples (see the inset of Fig. 10a) or occurring in a periodic arrangement (see the bottom panel of Fig. 10a). Some areas with a particularly high concentration of defects had about 10 defects per 100 nm^2 (Fig. 10b). All imaged defects appeared as depressions, the most predominant type observed on surfaces, and were considered to be Br vacancies. Using STM, Kim *et al.* revealed three kinds of PbI_2 vacancy defects with formation energies defined by $E_f = E_V - E_{SC} + \mu_C$, where E_V and E_{SC} are the total energy of the vacancy defect system and defect-free supercell structure, respectively, and μ_C is the chemical potential of PbI_2 or MAI.[131] The formation energies of PbI_2 vacancies based on the minimum energy configuration were calculated to be 27 meV, 73 meV, and 44 meV for A-type, B-type, and C-type, respectively (Fig. 10c). The MAI vacancy was formed by removing one CH_3NH_3 along with a nearby I atom. The formation energy of an MAI vacancy for the reference phase MAI molecule was estimated to be 1.803 eV. Meanwhile, PbI_2 vacancy formation energies were relatively lower than those of other semiconducting materials despite the variation of the actual formation energy with the concentration of the mixture. This confirmed the possible generation of abundant Schottky defects within the methylammonium lead halides (MALHs) absorber layer (Fig. 10d). Hieulle *et al.* successfully determined the exact location of I and Cl ions in mixed $CH_3NH_3PbBr_{3-y}I_y$ and $CH_3NH_3PbBr_{3-z}Cl_z$ perovskite lattices to clarify the formation of two different mixed-halide perovskites.[132] After the deposition of PbI_2 or $PbCl_2$ on pure $CH_3NH_3PbBr_3$, distinct protrusions with different apparent heights and widths appeared in STM images of perovskite films (Fig. 10e–g). Combining STM experimental results and DFT simulations, the dissociation of the PbI_2 (or $PbCl_2$) molecule followed by the substitution of Br by I (or Cl) at the surface of the perovskite film was confirmed. The bright and dark protrusions observed in the STM experiment were identified as I and Cl ions, respectively (Fig. 10h–k).

2.4 *In situ* characterization

During the fabrication of PSCs, external effects caused by the experimental procedures and operation methods would introduce defects into the MHP layer, causing its degradation. Since the growth/crystallization process of MHPs occurs at the atomic scale in nanoseconds, directly visualizing the formation of defects is often very challenging. Optical microscopy[133,134] can be used to track the growth/crystallization process of MHPs and provide some useful information but its low-resolution limit hinders its application for sample diameters of a few hundred nanometers. The growth/crystallization of MHPs is mainly based on a solution process, making the STM technique unsuitable. Consequently, *in situ* electron microscopy techniques and *in situ* spectrometry measurements have been updated to fit the dynamic micro-processes of MHPs.

2.4.1 *In situ* electron microscopy techniques. Recently, *in situ* electron microscopy techniques, such as transmission electron microscopy (TEM), have successfully been applied for direct observation of complex chemical reactions and material transformations, as well as charge flow in fuel cells, solar cells, and photocatalysis processes in real time. In addition to morphological observation by *in situ* TEM during operation, other comprehensive techniques like electron diffraction and electron energy loss spectroscopy (EELS) may provide information on local composition and structure. *In situ* TEM could reveal microstructural evolution, reaction kinetics, phase transitions, chemical changes, mechanical stress, and electrode/electrolyte interfaces using a liquid closed cell-based sample

 This journal is © The Royal Society of Chemistry 2022

holder combined with various imaging and analysis techniques. On the other hand, PSCs are often affected by temperature, electrical bias, and humidity to trigger various reactions, leading to the decomposition of MHPs. Therefore, the characterization and analysis of perovskite reactions under various conditions are necessary to clarify the factors hindering the device efficiency and stability. *In situ* TEM could reveal the atomic-level reactions of MHPs under different environmental conditions.

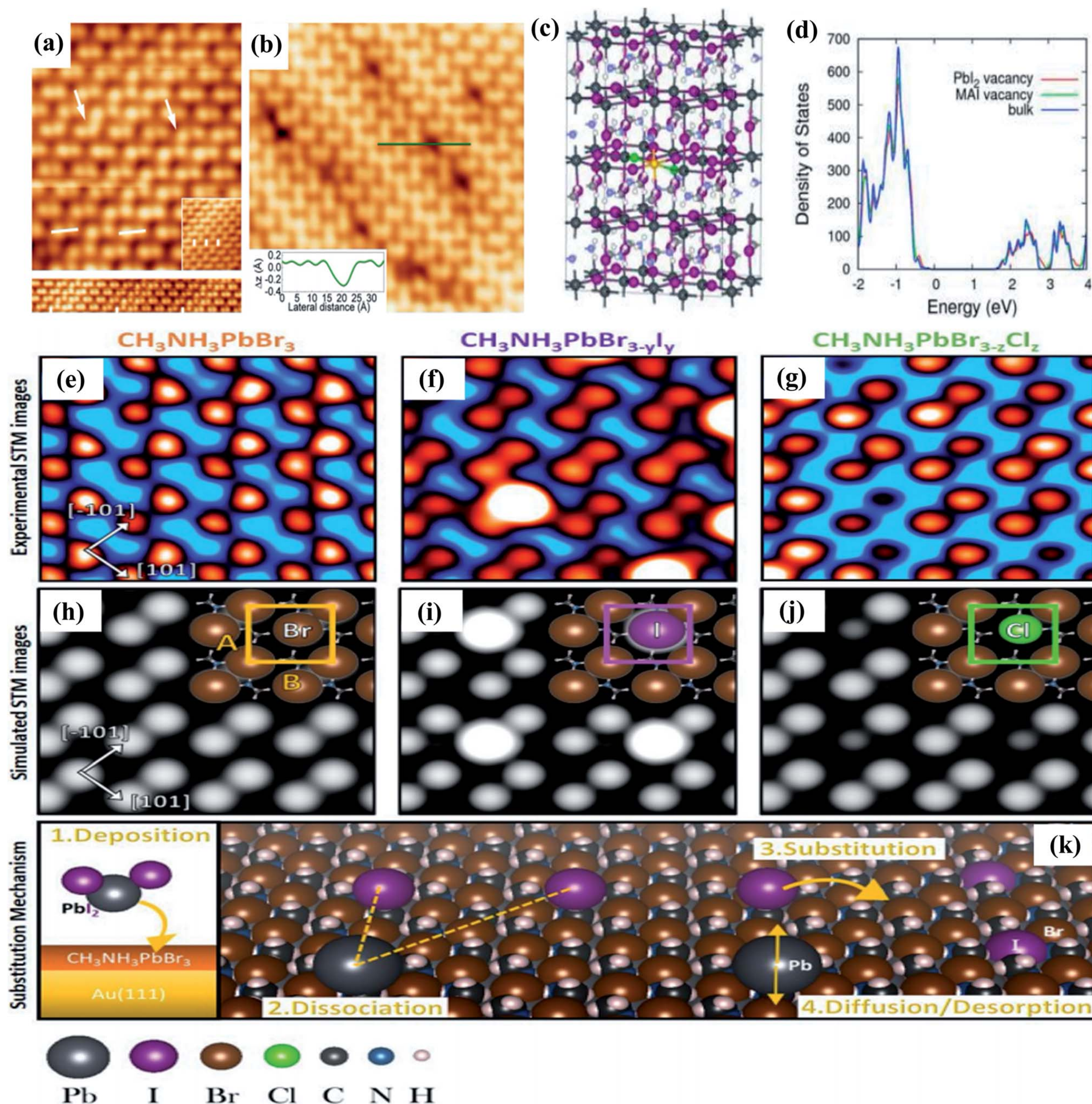

Fig. 10 Dislocations and defects visualized with STM. (a) Start of dislocation rows indicated by white arrows. The angled lines indicate the modified Br atom positions adjacent to a dislocation row. (b) STM image of defects on the surface. Reproduced with permission:[130] copyright 2015, American Chemical Society. (c) The position of the PbI_2 vacancy in the supercell of $CH_3NH_3PbI_3$. Vacant Pb and I are denoted by yellow and green, respectively. H, C, N, I, and Pb are represented by white, light gray, light blue, violet, and thick gray balls, respectively. (d) Density of states (DOS) for defect-free bulk $CH_3NH_3PbI_3$ and supercell structures having MAI and PbI_2 vacancies. Reproduced with permission:[131] copyright 2014, American Chemical Society. Scanning tunneling microscopy images of (e) $CH_3NH_3PbBr_3$, (f) $CH_3NH_3PbBr_{3-y}I_y$, and (g) $CH_3NH_3PbBr_{3-z}Cl_z$ perovskite surfaces. (h–j) Calculated (010) surface of the mixed halide organic–inorganic perovskites. (k) Scheme of the substitution mechanism occurring at the surface of the $CH_3NH_3PbBr_3$ perovskite after deposition of PbI_2 or $PbCl_2$ molecules (only the PbI_2 case is presented for clarity, but $PbCl_2$ follows the same mechanism). Reproduced with permission:[132] copyright 2019, American Chemical Society.

Published on 14 giugno 2022. Downloaded on 16/07/2024 00:14:22.

Published on 14 giugno 2022. Downloaded on 16/07/2024 00:14:22.

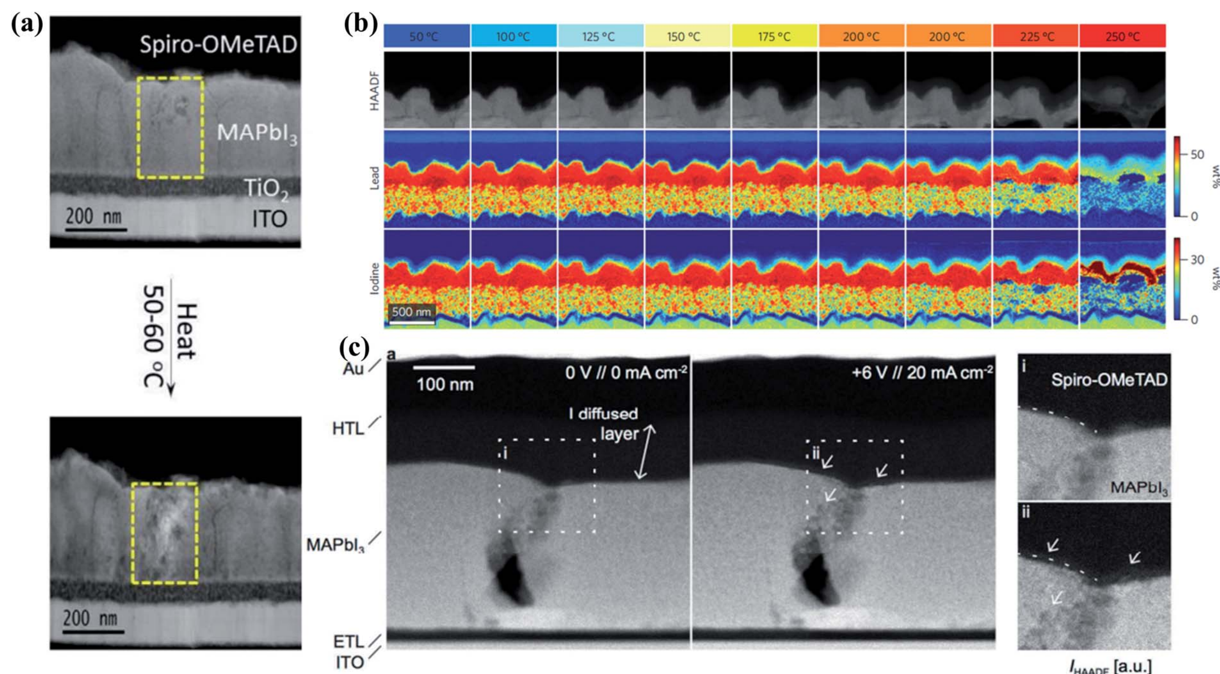

Fig. 11 (a) HAADF images for $MAPbI_3$ obtained from *in situ* TEM before heating (top) and after heating for 14 h (bottom). Reproduced with permission:[135] copyright 2016, American Chemical Society. (b) The evolution of the HAADF image, and lead and iodide compositions of the $MAPbI_3$ PSC depending on the temperature increase from 50 to 250 °C measured by *in situ* TEM observation for gradual thermal decomposition. Reproduced with permission:[136] copyright 2016, Springer Nature. (c) STEM HAADF micrographs showing changes in morphology of the $MAPbI_3$ layer when a current density of 20 mA cm^{-2} is passed through the cell with +6 V applied on the HTL, with (i) and (ii) showing magnified views of the regions highlighted in (c) (the dashed line represents the initial interface). Reproduced with permission:[70] copyright 2016, American Chemical Society.

Xiao *et al.* characterized non-encapsulated PSCs based on ITO/TiO_2/$MAPbI_3$/spiro-OMeTAD/Ag by *in situ* TEM heating in an effort to analyze the degradation process of $MAPbI_3$ during high-angle annular dark-field (HAADF) imaging (Fig. 11a).[135] The appearance of defects and fast degradation of $MAPbI_3$ after heating at ≈50–60 °C for 4 h demonstrated accelerated thermally induced elemental migration by Schottky or Frenkel defects in the $MAPbI_3$ crystal structure. These data provided an in-depth understanding of thermal degradation routes and microstructural changes of $MAPbI_3$ during decomposition. Ducati *et al.* used similar *in situ* TEM characterization at 150 °C on four samples composed of FTO/TiO_2/$MAPbI_3$/spiro-OMeTAD/Au fabricated by different routes.[136] The *in situ* monitoring of the morphological changes and chemical compositions by *in situ* heating during HAADF imaging and associated energy dispersive X-ray spectroscopy elemental mapping revealed (Fig. 11b) migration of iodine and lead into the spiro-MeOTAD HTL as the primary cause of $MAPbI_3$ degradation. Their work provided new insights into correlations between the morphology (perovskite coverage and scaffold infiltration), chemical composition (containing Cl or not), and thermal stability of perovskite materials. Shi *et al.* used *in situ* gas-cell TEM technology to explore the $MAPbI_3$ degradation mechanism. By controlling the atmosphere (vacuum or dry air) and temperature during *in situ* heating and gas-cell reaction (ATMOSPHERE 200 from Protochips), a surface-initiated layer-by-layer degradation model of $MAPbI_3$ was established under a simulated actual PSC operation environment in real time. *In situ* TEM is also suitable for use under electrical bias conditions. For instance, Jeangros *et al.* applied a positive bias on the HTL and noticed microstructural changes after a few minutes.[70] The changes in HAADF intensity with biasing showed continuous retraction of the $MAPbI_3$/HTL interface, while nanoparticles appeared at positions of structural defects and the interface with the HTL (Fig. 11c). The slight increase in the HAADF intensity in the HTL region in the vicinity of the $MAPbI_3$ phase under bias also indicated ionic migration of heavy elements, which induced the degradation of MHPs and caused the hysteresis effect of PSCs (arrowheads in the profiles in Fig. 11c).

2.4.2 *In situ* spectrometric measurement. Spectrometry-based techniques have good time resolution, and thus can be used to examine the growth/crystallization and annealing processes of MHPs for characterization of defects caused by experimental procedures and operation methods. Hu *et al.* investigated the natural drying kinetics of meniscus doctor blade-coated $Cs_{0.05}FA_{0.81}MA_{0.14}PbI_{2.55}Br_{0.45}$ perovskite precursor solution film in a N_2 filled glove box by time-resolved *in situ* UV-vis absorption spectroscopy.[137] Based on their results, classification of the solution stage, intermediate stage, and solid stage during the natural drying process was performed (Fig. 12a). Assisted by SEM and other measurements, they found that the nitrogen blowing at the intermediate phase (18 min) can lead to the uncovered regions as well as the pinholes in the $Cs_{0.05}FA_{0.81}MA_{0.14}PbI_{2.55}Br_{0.45}$ film. These film morphology

 This journal is © The Royal Society of Chemistry 2022

Published on 14 giugno 2022. Downloaded on 16/07/2024 00:14:22.

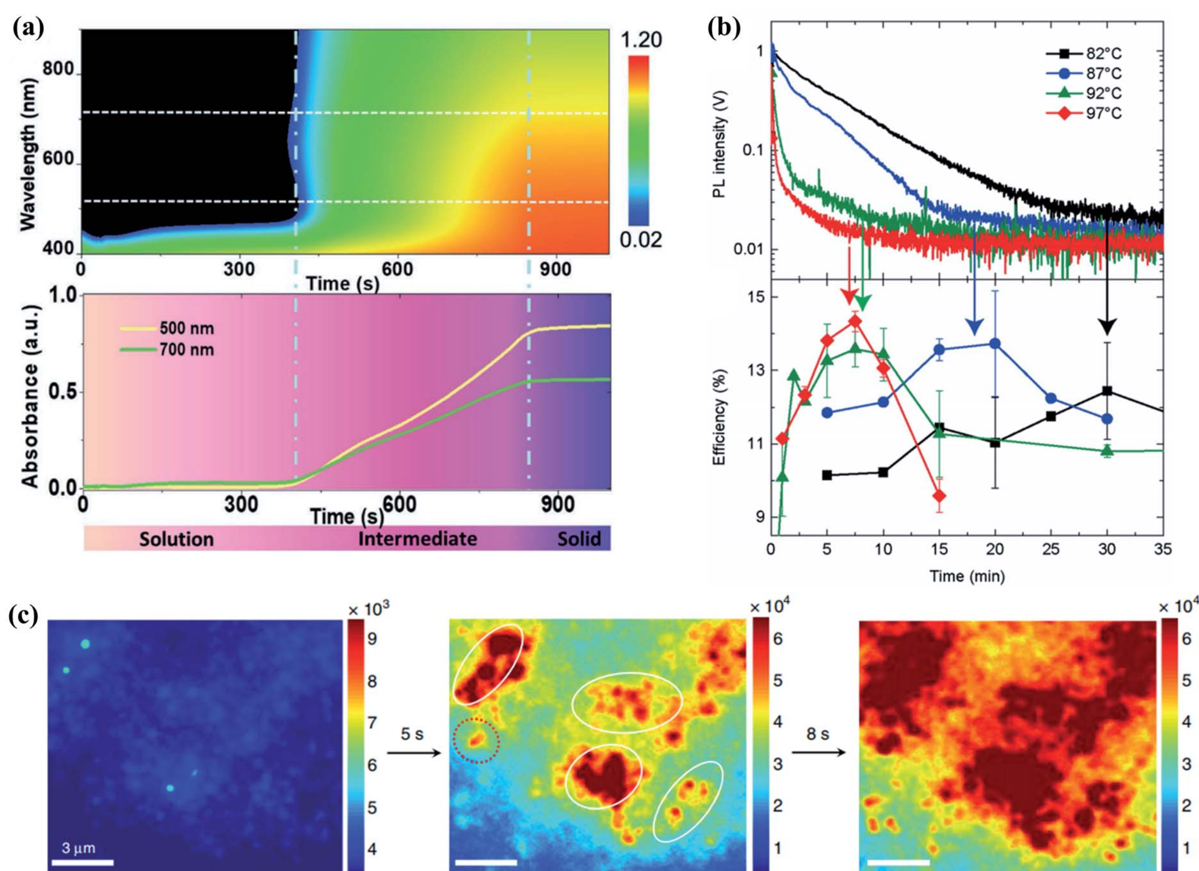

Fig. 12 (a) The upper part: Time-resolved *in situ* UV-vis absorption spectra of naturally dried $Cs_{0.05}FA_{0.81}MA_{0.14}PbI_{2.5}5Br_{0.45}$ perovskite film by meniscus coating. The bottom: time-resolved absorbance at the wavelengths of 500 and 700 nm, respectively. Reproduced with permission:[137] copyright 2019, Wiley-VCH. (b) Evolution of the PL intensity and correlated power conversion efficiency of the $MAPbI_3$ perovskite devices depending on the annealing temperature and the time. Reproduced with permission:[138] copyright 2016, Wiley-VCH. (c) PL imaging of the growth of perovskite seeded films. *In situ* photoluminescence microscopy reports real-time growth of perovskite from the preembedded perovskite seeds. The white circles indicate locations with perovskite-seed-assisted growth, while red dashed circles indicate locations with a random nucleation process. The color bar indicates the PL intensity emitted from the sample. Reproduced with permission:[139] copyright 2018, Springer Nature.

defects made bare SnO_2 come into direct contact with the hole-transporting layer (spiro-OMeTAD), which remarkably facilitates the surface charge recombination, and consequently causes the device performance to deteriorate. A relatively higher PCE was obtained with the nitrogen blowing at 0 min. Franeker *et al.* proposed that annealing improves charge transport, either due to an increased charge carrier mobility, or a lower amount of defects, or the fusion and growth of $MAPbI_3$ perovskite crystals. They measured the time evolution of photoluminescence intensities for four different annealing temperatures to pinpoint the optimal annealing time (Fig. 12b).[138] Their data revealed a strong influence of annealing temperature on the rate at which the photoluminescence intensity changed. During thermal annealing, the photoluminescence quenching and the solar cell efficiency increased due to an increase in the charge transport. Past the optimal annealing time, the formation of defects and a suboptimal stoichiometry of the $MAPbI_3$ perovskites resulted in a PCE decrease. The best device performance is achieved when the photoluminescence reaches its baseline value, and then the optimal annealing duration can be defined accordingly. Zhao *et al.* applied *in situ* PL imaging to investigate the $FAPbI_3$ perovskite crystallization process upon deposition of an organic ammonium salt solution onto seed-containing PbI_2 film by tracking the evolution of PL emission of the perovskite phase.[139] Two distinct types of growth kinetics were observed (perovskite-seed-assisted growth and random nucleation) (Fig. 12c, middle). Also, the perovskite-seed-assisted growth dominated the perovskite crystallization throughout the whole reaction process (Fig. 12c, right). The device performance characterization showed that planar solar cells based on $FAPbI_3$ films with perovskite seeding growth achieved relatively higher PCE and open-circuit voltage (V_{oc}). This perovskite seeding growth (PSG) method using Cs-containing perovskite seeds incorporates Cs cations into high-quality perovskite films, thereby achieving large grain sizes, low trap density, and quasi-single crystallographic orientation in $FAPbI_3$ films.

Published on 14 giugno 2022. Downloaded on 16/07/2024 00:14:22.

Table 1 Summary of the benefits and limitations of characterization measurements applied to probing defect passivation in PSCs

Characterization	Source	Benefits	Limitations	Ref.
TAS	Laser	• Detects both shallow and deep defects by tracing the junction capacitance • Provides E_A of defects • Measured on regular working devices under illumination	• Cannot distinguish between valence band and conduction band states • Only the defects below the energy demarcation can capture or emit charges and contribute to the capacitance signal • Trapped charges with long thermal emission time cannot contribute to the capacitance signal	79–90
DLCP	Electrical bias	• The spatial distribution of trap states can be deduced • Very high resolution	• Influenced by material surface roughness and uniformity • Susceptible to noise	36, 91 and 92
SCLC	Electrical bias	• Giving two types of defect density, *i.e.*, electron and hole density • E_A of the defects can be obtained by temperature-dependent SCLC	• Only shows a single type of defect density at one time • The kick point of V may not only be caused by the defect trap filling, but also by some other effects, which produce a deviation in the estimated defect density • Need to fabricate electron-only or hole-only devices	37, 38 and 93–99
TSC	Electric field Laser or rays	• Tracing of charge during trap filling and thermalization to detect defect levels • Provides defects to E_A	• Cannot directly measure charge on and within dielectrics • Defect density in MHPs can only be estimated minimally • A single TSC result is sometimes not informative	100–102
DLTS	Electrical bias	• Great sensitivity and wide range of observable defect depths • Providing information about E_A and electron- and hole-capture cross-sections	• Might miss minority carrier traps that cannot be saturated at practical levels of forward current • Cannot observe shallow-level defect traps with high thermal emission rate	39 and 103–105
ssPL	Pump	• Accurate estimates of total defect density • Volume and surface defect densities can also be calculated separately	• The energy level of the defect cannot be predicted • Defective E_A cannot be provided	40, 106 and 107
TA	Pump–probe	• Unlike in steady-state absorption spectroscopy, a transition of the signal occurs	• Data processing and analysis are more complex	76, 108 and 109
Photo-CELIV	Laser	• It can be used directly on operating devices • To simultaneously determine the charge carrier concentration and mobility	• Cannot distinguish the type of charge carrier	110–115
TRMC	Microwave electric field	• Contactless testing • Intrinsic charge carrier mobility can be evaluated with minimal trapping effects	• It is limited to the X-ray band. The frequency range is relatively narrow • Not applicable to devices with electrodes • The carrier problem of electrons and holes cannot be distinguished	116 and 117
TRFR/TRKR	Pump–probe	• Remarkable sensitivity to the spin sublevel transient filling of electrons and holes	• The detected weak signals are easily masked by various noises in the environment • The test integration time is too long, resulting in distortion of the signal under test	118–121
KPFM	Voltage	• Higher potential resolution • Non-contact testing does not damage the sample • It has broad application prospects in environmentally sensitive materials	• Dependence on distance • The AC bias voltage is limited and should not be too high	122–127

 This journal is © The Royal Society of Chemistry 2022

Published on 14 giugno 2022. Downloaded on 16/07/2024 00:14:22.

Table 1 (*Contd.*)

Characterization	Source	Benefits	Limitations	Ref.
DFT/STM	Electric current	• High atomic resolution	• Problems such as the particle size and uniformity of the conductive layer might limit the resolution of the image to the real surface	128–132
		• Can work in different environments such as vacuum, atmosphere, normal temperature, *etc.*	• STM characterization of full perovskite solar cell devices needs to be developed	
In situ TEM	Electron beam	• Dynamic imaging of the thermal degradation process of MHPs under different environmental conditions with high resolution	• Requirement for a special sample holder to simulate the actual operation of a full perovskite solar cell device • The *in situ* TEM characterization of PSCs under humid conditions needs to be developed • Atomic scale visualization of the dynamic micro-processes of MHPs has not been achieved	70, 135 and 136

3. Conclusion and outlook

Although the large-scale commercial application of PSCs has not yet been achieved, MHPs are still considered to be promising materials with potential use in various areas, and have thus continued to attract enthusiasm from researchers since being first reported in 2009. The recent rapid progress in high-PCE and large-area PSCs is inspiring, which is not only attributed to the effective material optimization strategies, but also the assistance of powerful characterization methods. Defect passivation has been confirmed to successfully reduce non-radiative charge recombination and ion migration in PSCs, as well as prevent the degradation of MHPs. Deep mechanistic insight into the fundamentals of defect characteristics and passivation physics of MHPs largely relied on suitable characterization techniques. In this article, several advanced characterization methods used for defect passivation were reviewed, including capacitance measurements (TAS, DLCP, SCLC, TSC and DLTS), spectrometry (ssPL, TA, photo-CELIV, TRMC, TRFR and TRKR) and microscopy (KPFM and STM) characterizations, and some newly applied *in situ* techniques (*in situ* TEM, time-resolved *in situ* UV-vis, and *in situ* PL imaging).

All methods showed great progress in gaining a better understanding of different micromechanisms in MHPs, conducive to the design and development of more efficient passivation methods. However, most techniques still showed limitations (Table 1). For example, during the TSC measurement, only trapped electrons which are continuously released through the thermal polarization process can generate I_{TSC} signals. Defect density in MHPs can only be minimally estimated. Compared to other characterization techniques, KPFM has high potential resolution and no required complex sample preparation. It is implemented in a non-contact manner, which greatly reduces sample damage. KPFM exhibited broad prospects in exploring the basic properties of environmentally sensitive materials and the operating mechanism of related devices. However, the distance dependence during testing indicates the effect of the interaction force on the KPFM. Also, the topography measurements at higher AC bias voltages can seriously influence the potential imaging. ssPL can be used to accurately estimate the total defect density, as well as calculate the volume and surface defect density separately. However, this method cannot be used to predict the defect energy level. TRMC technology is generally limited to the X-ray band, and the frequency range is relatively narrow. It cannot be applied to devices with electrodes due to technical limitations. Furthermore, detecting charge processes (electrons and holes) separately would be very challenging, as TRMC can only obtain the sum effects.

The rapid development of *in situ* TEM has provided an efficient approach for direct observation of electrochemical reactions and material degradation in MHPs. Detailed analysis of MHPs under realistic conditions could be crucial for understanding the key mechanisms of defect passivation and formulation of more efficient strategies to deal with various challenges in MHPs. Using *in situ* TEM, the perovskite atomic-scale degradation reactions can be correlated with actual environmental conditions, and changes of defects in MHPs can be observed. Thus, *in situ* TEM can be employed to deeply explore the thermal degradation mechanism of MHPs, and provide great guidance for optimizing the experiment approach to improve thermal stability. *In situ* spectroscopy can use full PSCs during operation to initially explore the defect mechanism. However, exploring defect generation and degradation mechanisms in PSCs under long-term operation is still a huge challenge. The sources of most high-energy detectors, such as lasers, electron beams or UV light, might interact with MHPs to accelerate ion migration, the phase transition and degradation at the extended testing time, which will hinder the accuracy of defect passivation characterization. In addition, the high sensitivity of MHPs to temperature and humidity would be prone to phase transition or degradation. Thus the strict control of the environmental conditions for testing might be important for obtaining the desired results.

Published on 14 giugno 2022. Downloaded on 16/07/2024 00:14:22.

In summary, the characterization tools of MHP research still require further optimization. The development of combined technologies of *in situ* spectrometry and *in situ* electron microscopy suitable for MHPs and PSCs will be a new urgent direction, in which simulation of the actual operation of PSCs, minimizing the effects of detector sources on MHPs, and reduction of the influences between each of the combined characterization tools remain challenging. In addition, combining *in situ* characterization with machine learning[140] would provide a more essential understanding of defect characteristics and passivation physics of MHPs towards highly efficient and long-term stable PSCs. Thus, continuous deepening of research on MHPs is also expected to promote the innovation of characterization technologies and instruments. Based on these efforts, a growing number of novel functional materials will be synthesized, and new advanced research methods for material characterization will be established in the future.

Author contributions

L. Wan conceived the idea, designed the structure of the review, revised the draft of the manuscript, supervised the work, and provided funding support. D. Cao and W. Li collected the papers related to the topic of the review. L. Wan, D. Cao and W. Li co-wrote the manuscript. X. Zhang, X. Wang and Z. Guo helped revise the manuscript. D. Eder and S. Wang provided funding support.

Conflicts of interest

There are no conflicts to declare.

Acknowledgements

I would like to thank the Editor and staff of the Journal of Materials Chemistry A for giving me the opportunity to publish an article. I would also like to take this opportunity to thank all the authors and referees for their effort and valuable time in composing and reviewing this article giving the readers some new perspectives on the current state-of-the-art advanced characterization techniques for probing defect passivation of PSCs. Finally, I would like to express my thankfulness for the financial support from all research funds: NSFC (51572072 and 21402045), Higher Education Discipline Innovation Project ("111 Project", D18025), Key Program for Intergovernmental S&T Innovation Cooperation Projects of National Key R&D Program of China (2019YFE0107100), Austria/China Scientific and Technological Cooperation (WTZ-OeAD CN03/2020), Hubei Provincial Department of Education (D20181005) and Department of Science and Technology of Hubei Province of China (2015CFA118 and 2014CFB167).

Notes and references

1 J.-W. Lee, S. Tan, S. Il Seok, Y. Yang and N.-G. Park, *Science*, 2022, **375**, eabj1186.
2 S. J. Woo, J. S. Kim and T. W. Lee, *Nat. Photonics*, 2021, **15**, 630–634.
3 L. Mei, R. Huang, C. Shen, J. Hu, P. Wang, Z. Xu, Z. Huang and L. Zhu, *Adv. Opt. Mater.*, 2022, **10**, 2102656.
4 Q.-M. Sun, J.-J. Xu, F.-F. Tao, W. Ye, C. Zhou, J.-H. He and J.-M. Lu, *Angew. Chem., Int. Ed.*, 2022, **4**, e202200872.
5 S. Deumel, B. A. Van, G. Gerwin, B. Peeters, J. Maas, R. Verbeek, S. Shanmugam, H. Akkerman, E. Meulenkamp, J. E. Huerdler, M. Acharya, M. García-Batlle, O. Almora, A. Guerrero, G. Garcia-Belmonte, W. Heiss, O. Schmidt and S. F. Tedde, *Nat. Electron. Mater.*, 2021, **4**, 681–688.
6 Y. Zhou, L. Zhao, Z. Ni, S. Xu, J. Zhao, X. Xiao and J. Huang, *Sci. Adv.*, 2021, **7**, 1–9.
7 A. J. J. M. van Breemen, R. Ollearo, S. Shanmugam, B. Peeters, L. C. J. M. Peters, R. L. van de Ketterij, I. Katsouras, H. B. Akkerman, C. H. Frijters, F. Di Giacomo, S. Veenstra, R. Andriessen, R. A. J. Janssen, E. A. Meulenkamp and G. H. Gelinck, *Nat. Electron.*, 2021, **4**, 818–826.
8 P. Chen, T. Li, Y. Yang, G. Li and X. Gao, *Nat. Commun.*, 2022, **13**, 64.
9 N. Tewari, S. B. Shivarudraiah and J. E. Halpert, *Nano Lett.*, 2021, **21**, 5578–5585.
10 Y. Dong, X. Tang, Z. Zhang, J. Song, T. Niu, D. Shan and H. Zeng, *Matter*, 2020, **3**, 273–286.
11 F. Bian, L. Sun, Y. Wang, D. Zhang, Z. Li and Y. Zhao, *Sci. China Chem.*, 2021, **64**, 1540–1546.
12 X. Sun, F. Zhang, L. Zhang, G. Liu, Y. Wang, Y. Wang and Y. Deng, *Soft Sci*, 2022, **2**, 1.
13 X. Song, H. Yin, Q. Chang, Y. Qian, C. Lyu, H. Min, X. Zong, C. Liu, Y. Fang, Z. Cheng, T. Qin, W. Huang and L. Wang, *Research*, 2021, **1**, 704–712.
14 M. C. Yen, C. J. Lee, K. H. Liu, Y. Peng, J. Leng, T. H. Chang, C. C. Chang, K. Tamada and Y. J. Lee, *Nat. Commun.*, 2021, **12**, 1–12.
15 C. Zhang, Y. Li, C. Ma and Q. Zhang, *Small Sci*, 2022, **2**, 2100086.
16 H. Min, D. Y. Lee, J. Kim, G. Kim, K. S. Lee, J. Kim, M. J. Paik, Y. K. Kim, K. S. Kim, M. G. Kim, T. J. Shin and S. Il Seok, *Nature*, 2021, **598**, 444–450.
17 C. Chen, X. Zhuang, W. Bi, Y. Wu, Y. Gao, G. Pan, D. Liu, Q. Dai and H. Song, *Nano Energy*, 2020, **68**, 104315.
18 L. Zhu, X. Zhang, M. Li, X. Shang, K. Lei, B. Zhang, C. Chen, S. Zheng, H. Song and J. Chen, *Adv. Energy Mater.*, 2021, **11**, 1–10.
19 Y. Jiang, X. Wang and A. Pan, *Adv. Mater.*, 2019, **31**, 1–47.
20 M. Vasilopoulou, A. Fakharuddin, A. G. Coutsolelos, P. Falaras, P. Argitis, A. R. B. M. Yusoff and M. K. Nazeeruddin, *Chem. Soc. Rev.*, 2020, **49**, 4496–4526.
21 Y. Lei, Y. Xu, M. Wang, G. Zhu and Z. Jin, *Small*, 2021, **17**, 1–26.
22 F. Gao, Y. Zhao, X. Zhang and J. You, *Adv. Energy Mater.*, 2020, **10**, 1902650.
23 Z. Ni, H. Jiao, C. Fei, H. Gu, S. Xu, Z. Yu, G. Yang, Y. Deng, Q. Jiang, Y. Liu, Y. Yan and J. Huang, *Nat. Energy*, 2022, **7**, 65–73.

 This journal is © The Royal Society of Chemistry 2022

Published on 14 giugno 2022. Downloaded on 16/07/2024 00:14:22.

24 T. A. S. Doherty, A. J. Winchester, S. Macpherson, D. N. Johnstone, V. Pareek, E. M. Tennyson, S. Kosar, F. U. Kosasih, M. Anaya, M. Abdi-Jalebi, Z. Andaji-Garmaroudi, E. L. Wong, J. Madéo, Y. H. Chiang, J. S. Park, Y. K. Jung, C. E. Petoukhoff, G. Divitini, M. K. L. Man, C. Ducati, A. Walsh, P. A. Midgley, K. M. Dani and S. D. Stranks, *Nature*, 2020, **580**, 360–366.
25 D. Luo, R. Su, W. Zhang, Q. Gong and R. Zhu, *Nat. Rev. Mater.*, 2020, **5**, 44–60.
26 H. Zhong, W. Li, Y. Huang, D. Cao, C. Zhang, H. Bao, Z. Guo, L. Wan, X. Zhang, X. Zhang, Y. Li, X. Ren, X. Wang, D. Eder, K. Wang, S. F. Liu and S. Wang, *ACS Appl. Mater. Interfaces*, 2022, **14**, 5183–5193.
27 B. Chen, P. N. Rudd, S. Yang, Y. Yuan and J. Huang, *Chem. Soc. Rev.*, 2019, **48**, 3842–3867.
28 Y. Xu, Y. Huang, H. Zhong, W. Li, D. Cao, C. Zhang, H. Bao, Z. Guo, L. Wan, X. Zhang, X. Zhang, Y. Li, X. Wang, D. Eder and S. Wang, *ACS Appl. Energy Mater.*, 2021, **4**, 11314–11324.
29 Y. Li, H. Wu, W. Qi, X. Zhou, J. Li, J. Cheng, Y. Zhao, Y. Li and X. Zhang, *Nano Energy*, 2020, **77**, 105237.
30 E. Rezaee, W. Zhang and S. R. P. Silva, *Small*, 2021, **17**, 1–18.
31 M. Xiao, L. Zhao, M. Geng, Y. Li, B. Dong, Z. Xu, L. Wan, W. Li and S. Wang, *Nanoscale*, 2018, **10**, 12141–12148.
32 N. J. Jeon, J. H. Noh, W. S. Yang, Y. C. Kim, S. Ryu, J. Seo and S. Il Seok, *Nature*, 2015, **517**, 476–480.
33 J. H. Noh, S. H. Im, J. H. Heo, T. N. Mandal and S. Il Seok, *Nano Lett.*, 2013, **13**, 1764–1769.
34 R. Fan, W. Zhou, Z. Huang and H. Zhou, *EnergyChem*, 2020, **2**, 100032.
35 M. cheol Kim, S. Y. Ham, D. Cheng, T. A. Wynn, H. S. Jung and Y. S. Meng, *Adv. Energy Mater.*, 2021, **11**, 1–26.
36 Z. Ni, C. Bao, Y. Liu, Q. Jiang, W. Wu, S. Chen, X. Dai, B. Chen, B. Hartweg, Z. Yu, Z. Holman and J. Huang, *Science*, 2020, **367**, 1352–1358.
37 G. Malliaras, J. Salem, P. Brock and C. Scott, *Phys. Rev. B: Condens. Matter Mater. Phys.*, 1998, **58**, R13411–R13414.
38 D. Shi, V. Adinolfi, R. Comin, M. Yuan, E. Alarousu, A. Buin, Y. Chen, S. Hoogland, A. Rothenberger, K. Katsiev, Y. Losovyj, X. Zhang, P. A. Dowben, O. F. Mohammed, E. H. Sargent and O. M. Bakr, *Science*, 2015, **347**, 519–522.
39 S. Reichert, J. Flemming, Q. An, Y. Vaynzof, J. F. Pietschmann and C. Deibel, *Phys. Rev. Appl.*, 2020, **13**, 034018.
40 F. Yuan, Z. Wu, H. Dong, J. Xi, K. Xi, G. Divitini, B. Jiao, X. Hou, S. Wang and Q. Gong, *J. Phys. Chem. C*, 2017, **121**, 15318–15325.
41 A. A. Eliwi, M. Malekshahi Byranvand, P. Fassl, M. R. Khan, I. M. Hossain, M. Frericks, S. Ternes, T. Abzieher, J. A. Schwenzer, T. Mayer, J. P. Hofmann, B. S. Richards, U. Lemmer, M. Saliba and U. W. Paetzold, *J. Mater. Chem. A*, 2022, **3**, 456–466.
42 C. Ran, J. Xu, W. Gao, C. Huang and S. Dou, *Chem. Soc. Rev.*, 2018, **47**, 4581–4610.
43 X. Qiu, Y. Liu, W. Li and Y. Hu, *Nanoscale*, 2020, **12**, 22425–22451.
44 J. M. Ball and A. Petrozza, *Nat. Energy*, 2016, **1**, 16149.
45 W. J. Yin, T. Shi and Y. Yan, *Appl. Phys. Lett.*, 2014, **104**, 1312–1317.
46 N. Liu and C. Y. Yam, *Phys. Chem. Chem. Phys.*, 2018, **20**, 6800–6804.
47 Y. Li, C. Zhang, X. Zhang, D. Huang, Q. Shen, Y. Cheng and W. Huang, *Appl. Phys. Lett.*, 2017, **111**, 162106.
48 Y. Huang, W. J. Yin and Y. He, *J. Phys. Chem. C*, 2018, **122**, 1345–1350.
49 S. P. Dunfield, L. Bliss, F. Zhang, J. M. Luther, K. Zhu, M. F. A. M. van Hest, M. O. Reese and J. J. Berry, *Adv. Energy Mater.*, 2020, **10**, 1904054.
50 J. Kang and L. W. Wang, *J. Phys. Chem. Lett.*, 2017, **8**, 489–493.
51 P. Xu, S. Chen, H. J. Xiang, X. G. Gong and S. H. Wei, *Chem. Mater.*, 2014, **26**, 6068–6072.
52 D. Meggiolaro, S. G. Motti, E. Mosconi, A. J. Barker, J. Ball, C. Andrea Riccardo Perini, F. Deschler, A. Petrozza and F. De Angelis, *Energy Environ. Sci.*, 2018, **11**, 702–713.
53 T. Shi, H. S. Zhang, W. Meng, Q. Teng, M. Liu, X. Yang, Y. Yan, H. L. Yip and Y. J. Zhao, *J. Mater. Chem. A*, 2017, **5**, 15124–15129.
54 K. X. Steirer, P. Schulz, G. Teeter, V. Stevanovic, M. Yang, K. Zhu and J. J. Berry, *ACS Energy Lett.*, 2016, **1**, 360–366.
55 A. Walsh, D. O. Scanlon, S. Chen, X. G. Gong and S. H. Wei, *Angew. Chem., Int. Ed.*, 2015, **54**, 1791–1794.
56 Z. Li, C. Xiao, Y. Yang, S. P. Harvey, D. H. Kim, J. A. Christians, M. Yang, P. Schulz, S. U. Nanayakkara, C. S. Jiang, J. M. Luther, J. J. Berry, M. C. Beard, M. M. Al-Jassim and K. Zhu, *Energy Environ. Sci.*, 2017, **10**, 1234–1242.
57 K. Domanski, J. P. Correa-Baena, N. Mine, M. K. Nazeeruddin, A. Abate, M. Saliba, W. Tress, A. Hagfeldt and M. Grätzel, *ACS Nano*, 2016, **10**, 6306–6314.
58 R. Long, J. Liu and O. V. Prezhdo, *J. Am. Chem. Soc.*, 2016, **138**, 3884–3890.
59 X. Wu, M. T. Trinh, D. Niesner, H. Zhu, Z. Norman, J. S. Owen, O. Yaffe, B. J. Kudisch and X. Y. Zhu, *J. Am. Chem. Soc.*, 2015, **137**, 2089–2096.
60 W. Zhang, S. Pathak, N. Sakai, T. Stergiopoulos, P. K. Nayak, N. K. Noel, A. A. Haghighirad, V. M. Burlakov, D. W. Dequilettes, A. Sadhanala, W. Li, L. Wang, D. S. Ginger, R. H. Friend and H. J. Snaith, *Nat. Commun.*, 2015, **6**, 1–9.
61 G. Sadoughi, D. E. Starr, E. Handick, S. D. Stranks, M. Gorgoi, R. G. Wilks, M. Bär and H. J. Snaith, *ACS Appl. Mater. Interfaces*, 2015, **7**, 13440–13444.
62 M. Pitaro, E. K. Tekelenburg, S. Shao and M. A. Loi, *Adv. Mater.*, 2022, **34**, 2105844.
63 F. Paquin, J. Rivnay, A. Salleo, N. Stingelin and C. Silva, *J. Mater. Chem. C*, 2015, **3**, 10715–10722.
64 S. Zhang, Z. Liu, W. Zhang, Z. Jiang, W. Chen, R. Chen, Y. Huang, Z. Yang, Y. Zhang, L. Han and W. Chen, *Adv. Energy Mater.*, 2020, **10**, 1–49.
65 E. Bi, H. Chen, F. Xie, Y. Wu, W. Chen, Y. Su, A. Islam, M. Grätzel, X. Yang and L. Han, *Nat. Commun.*, 2017, **8**, 1–7.
66 Y. Cheng, X. Xu, Y. Xie, H. W. Li, J. Qing, C. Ma, C. S. Lee, F. So and S. W. Tsang, *Sol. RRL*, 2017, **1**, 1–8.

Published on 14 giugno 2022. Downloaded on 16/07/2024 00:14:22.

67 F. Bella, G. Griffini, J. P. Correa-Baena, G. Saracco, M. Grätzel, A. Hagfeldt, S. Turri and C. Gerbaldi, *Science*, 2016, **354**, 203–206.
68 D. W. DeQuilettes, W. Zhang, V. M. Burlakov, D. J. Graham, T. Leijtens, A. Osherov, V. Bulović, H. J. Snaith, D. S. Ginger and S. D. Stranks, *Nat. Commun.*, 2016, **7**, 11683.
69 M. Cherasse, J. Dong, G. Trippé-Allard, E. Deleporte, D. Garrot, S. F. Maehrlein, M. Wolf, Z. Chen, E. Papalazarou, M. Marsi, J.-P. Rueff, A. Taleb-Ibrahimi and L. Perfetti, *Nano Lett.*, 2022, **22**, 2065–2069.
70 Q. Jeangros, M. Duchamp, J. Werner, M. Kruth, R. E. Dunin-Borkowski, B. Niesen, C. Ballif and A. Hessler-Wyser, *Nano Lett.*, 2016, **16**, 7013–7018.
71 A. Ray, B. Martín-García, A. Moliterni, N. Casati, K. M. Boopathi, D. Spirito, L. Goldoni, M. Prato, C. Giacobbe, C. Giannini, F. Di Stasio, R. Krahne, L. Manna and A. L. Abdelhady, *Adv. Mater.*, 2022, **34**, 1–11.
72 Z. Chen, B. Turedi, A. Y. Alsalloum, C. Yang, X. Zheng, I. Gereige, A. Alsaggaf, O. F. Mohammed and O. M. Bakr, *ACS Energy Lett.*, 2019, **4**, 1258–1259.
73 C. Wu, H. Li, Y. Yan, B. Chi, J. Pu, J. Li, M. Sanghadasa and S. Priya, *Nano Energy*, 2017, **36**, 295–302.
74 J. Liu, J. Leng, K. Wu, J. Zhang and S. Jin, *J. Am. Chem. Soc.*, 2017, **139**, 1432–1435.
75 X. Liu, Z. Yu, T. Wang, K. L. Chiu, F. Lin, H. Gong, L. Ding and Y. Cheng, *Adv. Energy Mater.*, 2020, **10**, 1–9.
76 T. Wang, Y. Fu, L. Jin, S. Deng, D. Pan, L. Dong, S. Jin and L. Huang, *J. Am. Chem. Soc.*, 2020, **142**, 16254–16264.
77 Y. Wang, Y. Liu, Y. Xu, C. Zhang, H. Bao, J. Wang, Z. Guo, L. Wan, D. Eder and S. Wang, *Electrochim. Acta*, 2020, **329**, 135173.
78 Y. Zong, Y. Zhou, Y. Zhang, Z. Li, L. Zhang, M. G. Ju, M. Chen, S. Pang, X. C. Zeng and N. P. Padture, *Chem*, 2018, **4**, 1404–1415.
79 T. Walter, R. Herberholz, C. Müller and H. W. Schock, *J. Appl. Phys.*, 1996, **80**, 4411–4420.
80 H. S. Duan, H. Zhou, Q. Chen, P. Sun, S. Luo, T. Bin Song, B. Bob and Y. Yang, *Phys. Chem. Chem. Phys.*, 2015, **17**, 112–116.
81 Q. Dong, Y. Fang, Y. Shao, P. Mulligan, J. Qiu, L. Cao and J. Huang, *Science*, 2015, **347**, 967–970.
82 Y. Shao, Z. Xiao, C. Bi, Y. Yuan and J. Huang, *Nat. Commun.*, 2014, **5**, 1–7.
83 T. Kirchartz, W. Gong, S. A. Hawks, T. Agostinelli, R. C. I. MacKenzie, Y. Yang and J. Nelson, *J. Phys. Chem. C*, 2012, **116**, 7672–7680.
84 S. Ye, H. Rao, Z. Zhao, L. Zhang, H. Bao, W. Sun, Y. Li, F. Gu, J. Wang, Z. Liu, Z. Bian and C. Huang, *J. Am. Chem. Soc.*, 2017, **139**, 7504–7512.
85 C. Chen, Z. Song, C. Xiao, R. A. Awni, C. Yao, N. Shrestha, C. Li, S. S. Bista, Y. Zhang, L. Chen, R. J. Ellingson, C. S. Jiang, M. Al-Jassim, G. Fang and Y. Yan, *ACS Energy Lett.*, 2020, **5**, 2560–2568.
86 X. Zheng, B. Chen, J. Dai, Y. Fang, Y. Bai, Y. Lin, H. Wei, X. C. Zeng and J. Huang, *Nat. Energy*, 2017, **2**, 1–9.
87 L. Zhang, X. Zhou, X. Zhong, C. Cheng, Y. Tian and B. Xu, *Nano Energy*, 2019, **57**, 248–255.
88 W. Li, W. Zhang, S. Van Reenen, R. J. Sutton, J. Fan, A. A. Haghighirad, M. B. Johnston, L. Wang and H. J. Snaith, *Energy Environ. Sci.*, 2016, **9**, 490–498.
89 J. F. Liao, W. Q. Wu, J. X. Zhong, Y. Jiang, L. Wang and D. Bin Kuang, *J. Mater. Chem. A*, 2019, **7**, 9025–9033.
90 Y. Lin, B. Chen, F. Zhao, X. Zheng, Y. Deng, Y. Shao, Y. Fang, Y. Bai, C. Wang and J. Huang, *Adv. Mater.*, 2017, **29**, 1–8.
91 H. S. Pang, H. Xu, C. Tang, L. K. Meng, Y. Ding, H. T. Cai, J. Xiao, R. L. Liu, W. Q. Zeng and W. Huang, *J. Phys. Chem. C*, 2019, **123**, 165–174.
92 C. W. Warren, E. T. Roe, D. W. Miller, W. N. Shafarman and M. C. Lonergan, *Appl. Phys. Lett.*, 2017, **110**, 203901.
93 R. H. Bube, *J. Appl. Phys.*, 1962, **33**, 1733–1737.
94 D. Ju, X. Jiang, H. Xiao, X. Chen, X. Hu and X. Tao, *J. Mater. Chem. A*, 2018, **6**, 20753–20759.
95 Y. Zhang, M. Sun, N. Zhou, B. Huang and H. Zhou, *J. Phys. Chem. Lett.*, 2020, **11**(18), 7610–7616.
96 C. Zhang, K. Wang, Y. Wang, W. S. Subhani, X. Jiang, S. Wang, H. Bao, L. Liu, L. Wan and S. Liu, *Sol. RRL*, 2020, **4**, 2000254.
97 Y. Wang, K. Wang, W. S. Subhani, C. Zhang, X. Jiang, S. Wang, H. Bao, L. Liu, L. Wan and S. Liu, *Small*, 2020, **16**, 1–10.
98 Z. Ye, J. Zhou, J. Hou, F. Deng, Y. Z. Zheng and X. Tao, *Sol. RRL*, 2019, **3**, 1900109.
99 N. Liu, P. Liu, H. Zhou, Y. Bai and Q. Chen, *J. Phys. Chem. Lett.*, 2020, **11**, 3521–3528.
100 R. Schmechel and H. Von Seggern, *Phys. Status Solidi Appl. Res.*, 2004, **201**, 1215–1235.
101 J. Schafferhans, A. Baumann, C. Deibel and V. Dyakonov, *Appl. Phys. Lett.*, 2008, **93**, 1–4.
102 A. Baumann, S. Väth, P. Rieder, M. C. Heiber, K. Tvingstedt and V. Dyakonov, *J. Phys. Chem. Lett.*, 2015, **6**, 2350–2354.
103 D. V. Lang, *J. Appl. Phys.*, 1974, **45**, 3023–3032.
104 J. W. Rosenberg, M. J. Legodi, Y. Rakita, D. Cahen and M. Diale, *J. Appl. Phys.*, 2017, **122**, 145701.
105 A. Y. Polyakov, N. B. Smirnov, I. V. Shchemerov, D. S. Saranin, T. S. Le, S. I. Didenko, D. V. Kuznetsov, A. Agresti, S. Pescetelli, F. Matteocci and A. Di Carlo, *Appl. Phys. Lett.*, 2018, **113**, 263501.
106 P. Uhd Jepsen, W. Schairer, I. H. Libon, U. Lemmer, N. E. Hecker, M. Birkholz, K. Lips and M. Schall, *Appl. Phys. Lett.*, 2001, **79**, 1291–1293.
107 G. Xing, N. Mathews, S. S. Lim, N. Yantara, X. Liu, D. Sabba, M. Grätzel, S. Mhaisalkar and T. C. Sum, *Nat. Mater.*, 2014, **13**, 476–480.
108 J. M. Snaider, Z. Guo, T. Wang, M. Yang, L. Yuan, K. Zhu and L. Huang, *ACS Energy Lett.*, 2018, **3**, 1402–1408.
109 Z. Li, B. Ma, Y. Xu, Y. Lei, W. Lan, G. Wang, W. Li, Q. Wang, H. L. Zhang and Z. Jin, *Adv. Funct. Mater.*, 2021, **31**, 2106380.
110 G. Juska, K. Arlauskas and M. Viliunas, *Phys. Rev. Lett.*, 2000, **84**, 4946–4949.
111 D. A. R. Barkhouse, O. Gunawan, T. Gokmen, T. K. Todorov and D. B. Mitzi, *Prog. Photovoltaics Res. Appl.*, 2007, **15**, 677–696.

 This journal is © The Royal Society of Chemistry 2022

Published on 14 giugno 2022. Downloaded on 16/07/2024 00:14:22.

112 O. J. Sandberg and M. Nyman, *Org. Electron.*, 2019, **64**, 97–103.
113 M. Stephen, S. Karuthedath, T. Sauermann, K. Genevičius and G. Juška, *Proc. of SPIE*, 2014, **9184**, 918424.
114 M. Petrović, T. Ye, C. Vijila and S. Ramakrishna, *Adv. Energy Mater.*, 2017, **7**, 1602610.
115 Y. Chen, J. Peng, D. Su, X. Chen and Z. Liang, *ACS Appl. Mater. Interfaces*, 2015, **7**, 4471–4475.
116 J. Xu, C. C. Boyd, Z. J. Yu, A. F. Palmstrom, D. J. Witter, B. W. Larson, R. M. France, J. Werner, S. P. Harvey, E. J. Wolf, W. Weigand, S. Manzoor, M. F. A. M. Van Hest, J. J. Berry, J. M. Luther, Z. C. Holman and M. D. McGehee, *Science*, 2020, **367**, 1097–1104.
117 H. Oga, A. Saeki, Y. Ogomi, S. Hayase and S. Seki, *J. Am. Chem. Soc.*, 2014, **136**, 13818–13825.
118 T. Adachi, Y. Ohno, R. Terauchi, F. Matsukura and H. Ohno, *Phys. E Low Dimens. Syst. Nanostruct.*, 2000, **7**, 1015–1019.
119 L. S. Liu, W. X. Wang, Z. H. Li, B. L. Liu, H. M. Zhao, J. Wang, H. C. Gao, Z. W. Jiang, S. Liu, H. Chen and J. M. Zhou, *J. Cryst. Growth*, 2007, **301–302**, 93–96.
120 D. Giovanni, H. Ma, J. Chua, M. Grätzel, R. Ramesh, S. G. Mhaisalkar, N. Mathews and T. C. Sum, *Nano Lett.*, 2015, **15**(3), 1553–1558.
121 Z. Liu, J. Hu, H. Jiao, L. Li, G. Zheng, Y. Chen, Y. Huang, Q. Zhang, C. Shen, Q. Chen and H. Zhou, *Adv. Mater.*, 2017, **29**, 1–8.
122 N. Faraji, C. Qin, T. Matsushima, C. Adachi and J. Seidel, *J. Phys. Chem. C*, 2018, **122**, 4817–4821.
123 K. Song, Y. Wu, X. Chen, Y. He, L. Liu, G. Chen and R. Liu, *AIP Adv*, 2018, **8**, 035114.
124 Z. Kang, H. Si, M. Shi, C. Xu, W. Fan, S. Ma, A. Kausar, Q. Liao, Z. Zhang and Y. Zhang, *Sci. China Mater.*, 2019, **62**, 776–789.
125 W. Melitz, J. Shen, A. C. Kummel and S. Lee, *Surf. Sci. Rep.*, 2011, **66**, 1–27.
126 S. Tan, J. Shi, B. Yu, W. Zhao, Y. Li, Y. Li, H. Wu, Y. Luo, D. Li and Q. Meng, *Adv. Funct. Mater.*, 2021, **31**, 1–10.
127 M. Li, X. Yan, Z. Kang, X. Liao, Y. Li, X. Zheng, P. Lin, J. Meng and Y. Zhang, *ACS Appl. Mater. Interfaces*, 2017, **9**, 7224–7231.
128 L. K. Ono and Y. Qi, *J. Phys. Chem. Lett.*, 2016, **7**, 4764–4794.
129 S. Wang, T. Sakurai, W. Wen and Y. Qi, *Adv. Mater. Interfaces*, 2018, **5**, 1–30.
130 R. Ohmann, L. K. Ono, H. S. Kim, H. Lin, M. V. Lee, Y. Li, N. G. Park and Y. Qi, *J. Am. Chem. Soc.*, 2015, **137**, 16049–16054.
131 J. Kim, S.-H. Lee, J. H. Lee and K.-H. Hong, *J. Phys. Chem. Lett.*, 2014, **5**, 1312–1317.
132 J. Hieulle, X. Wang, C. Stecker, D. Y. Son, L. Qiu, R. Ohmann, L. K. Ono, A. Mugarza, Y. Yan and Y. Qi, *J. Am. Chem. Soc.*, 2019, **141**, 3515–3523.
133 J. Li, R. Munir, Y. Fan, T. Niu, Y. Liu, Y. Zhong, Z. Yang, Y. Tian, B. Liu, J. Sun, D. M. Smilgies, S. Thoroddsen, A. Amassian, K. Zhao and S. Liu, *Joule*, 2018, **2**, 1313–1330.
134 M. He, B. Li, X. Cui, B. Jiang, Y. He, Y. Chen, D. O'Neil, P. Szymanski, M. A. Ei-Sayed, J. Huang and Z. Lin, *Nat. Commun.*, 2017, **8**, 16045.
135 B. Yang, O. Dyck, W. Ming, M. H. Du, S. Das, C. M. Rouleau, G. Duscher, D. B. Geohegan and K. Xiao, *ACS Appl. Mater. Interfaces*, 2016, **8**, 32333–32340.
136 G. Divitini, S. Cacovich, F. Matteocci, L. Cinà, A. Di Carlo and C. Ducati, *Nat. Energy*, 2016, **1**, 15012.
137 H. Hu, Z. Ren, P. W. K. Fong, M. Qin, D. Liu, D. Lei, X. Lu and G. Li, *Adv. Funct. Mater.*, 2019, **29**, 1–12.
138 J. J. van Franeker, K. H. Hendriks, B. J. Bruijnaers, M. W. G. M. Verhoeven, M. M. Wienk and R. A. J. Janssen, *Adv. Energy Mater.*, 2017, **7**, 1–9.
139 Y. Zhao, H. Tan, H. Yuan, Z. Yang, J. Z. Fan, J. Kim, O. Voznyy, X. Gong, L. N. Quan, C. S. Tan, J. Hofkens, D. Yu, Q. Zhao and E. H. Sargent, *Nat. Commun.*, 2018, **9**, 1–10.
140 K. Higgins, M. Lorenz, M. Ziatdinov, R. K. Vasudevan, A. V. Ievlev, E. D. Lukosi, O. S. Ovchinnikova, S. V. Kalinin and M. Ahmadi, *Adv. Funct. Mater.*, 2020, **30**, 1–11.
141 Y. Wu, W. Chen, Z. Wan, A. B. Djurišić, X. Feng, L. Liu, G. Chen, R. Liu and Z. He, *J. Power Sources*, 2019, **425**, 130–137.